

# Modeling mechanochemical coupling in cell polarity establishment

Ondrej Maxian

November 17, 2023

This project is about understanding the design principles by which cells combine mechanics (the actomyosin network) and biochemistry to robustly polarize.

## 1 Introduction and literature review

Cell polarity is essential for many aspects of organismal development and physiology, including stem cell dynamics, directional cell migration, and asymmetric cell division [6, 13, 17, 24]. On a large scale, a cell’s polarity state is encoded by asymmetric distributions of protein molecules, which are shaped by smaller-scale processes like binding, diffusion, and active transport. The key group of proteins involved in this process are the so-called PAR proteins, which are highly conserved across the metazoa, and are typically distributed asymmetrically during cell division [19, 22] in the presence of actomyosin-mediated contractile flows [27].

The one-cell *C. elegans* embryo is one of the premier model systems for polarization in eukaryotic cells. In this system, polarity is encoded by the distribution of two distinct groups of polarity proteins: anterior PARs (aPARs), which include PAR-3, PAR-6/PKC-3, and CDC-42, and posterior PARs (pPARs), which include PAR-2, PAR-1, LGL-1, and CHIN-1 [22]. Wild-type embryos polarize in two distinct phases termed “establishment” and “maintenance” [3]. In establishment phase, a local sperm cue at the anterior pole acts to load PAR-2 onto the membrane, while at the same time promoting strong anterior-directed actomyosin flows [10]. These cues, together with the mutual inhibition of the aPAR and pPAR domain, sort the PAR proteins into their respective domains, where they are then maintained during maintenance phase [27, 31].

In the language of dynamical systems, it can therefore be said that the *C. elegans* embryo possesses two stable states: a uniform state, in which all of the proteins are distributed symmetrically throughout the cell, and a polarized state, in which the PAR proteins are sorted into their respective domains. The switch between the two states is then governed by the sperm cue, which drives

an advective flow to trigger a switch between the two states [12, 14]. Indeed, recent theoretical and experimental studies showed that the cell operates in a regime where cues are necessary to establish polarity, thus avoiding the potentially chaotic case of spontaneous polarization without cues.

This analysis suggests that cue-driven flows are required for polarity establishment, and that flow patterns PAR proteins. Yet, it has been demonstrated repeatedly that embryos lacking a functional flow during establishment phase still polarize, albeit in a delayed manner, and furthermore find the same boundary position as embryos with a functional establishment-phase flow [35, 34]. The flows in these embryos result from a switch from rho-dependent contractility in establishment phase to CDC-42-dependent contractility in maintenance phase [31]. Still though, absent the cue the PAR proteins are the only agents that could pattern actomyosin flows. Thus, these “maintenance-phase” rescue experiments hint that PAR proteins pattern flows, rather than the other way around. This gets at the general question: what are the design principles by which cells combine the PAR protein circuit with actomyosin to robustly encode a dynamically stable polarity state with a fixed boundary position?

Because of the complexity of the *in vivo* system, a definitive answer to this question is only possible with a combination of experiments and modeling. This fact was recognized early on in the field, and indeed there is no dearth of models in the literature (see [32, 5, 4, 11, 14, 12, 20] for a subset). In early models, *potential* mechanics for polarization were explored, but the relative abundance of experimental data in the last decade can allow us to be more precise. For example, an early model of Tostevin and Howard showed that polarity sorting could occur if actomyosin flows feedback onto the aPAR [32] but not pPAR distribution, but recent experiments have shown that both cortical aPARs and pPARs are transported by myosin [18]. We do not take the harsh view that these early models are incorrect; rather, we view them as missing some fundamental biochemistry that was at the time unknown. Consequently, our goal here is to construct a minimal model based on existing experimental evidence that shows how the combination of aPAR/pPAR mutual inhibition and actomyosin flows generate a stable polarity state with fixed boundary position. There are two fundamental questions that we need to answer in constructing the model: first, what is the nature of the aPAR/pPAR mutual inhibition, and is it sufficient to encode a stable polarity state on its own? And second, how do the PAR proteins impact contractility?

With regard to mutual inhibition, it is known that asymmetries in the PAR proteins are stable once set up if myosin is removed [30], which demonstrates that mutual inhibition on its own is sufficient for bistability. Yet, how this mutual inhibition works is unclear. The main source of

the confusion is that simple first-order mass action kinetics, wherein proteins  $A$  and  $P$  inhibit each other via a term proportional to  $AP$ , is guaranteed *not* to generate bistability, so some other assumption must be made to obtain it. Absent other compelling explanations, some models choose stoichiometric reaction terms to guarantee bistability [12, 14], but do not impart any insight into the molecular mechanism by which this occurs.

There has been a large amount of modeling and experimental work [5, 7, 23, 21] on how the oligomerization of PAR-3 contributes to bistability. It is known that disrupting PAR-3 [9] or its oligomerization [7] leads to a failure or severe disruption in establishing polarity. It was recently shown that PAR-3 asymmetries are stable even in the absence of its posterior inhibitor PAR-1, which suggest that the dynamics of PAR-3 *by itself* are intrinsically bistable [21], and might therefore “anchor” the bistability of the entire PAR protein system. Experimental evidence has shown that the bistability occurs via a mechanism in which membrane-bound PAR-3 recruits additional cytoplasmic monomers to the membrane, which is not captured in previous models which show a drifting boundary [5]. In this work, we will therefore consider a model in which positive feedback endows the PAR-3 system with intrinsic bistability, which is amplified by first order mutual inhibition with posterior PARs. Our treatment is based strongly on that of Lang and Munro [23], but is distinct in that we argue for *bistability* (described by them as “inducible polarization”) rather than spontaneous *instability*. Our first order treatment of aPAR/pPAR interactions is not meant to exclude possible nonlinearities in the mutual inhibition, but rather to show that intrinsic bistability of PAR-3 can combine with the simplest possible inhibition kinetics to yield bistability.

Once we set up a bistable reaction system, the question becomes how we can move from the uniform to the polarized state. Experiments suggest that there are two intrinsic boundary positions here: one (at about 75% egg length) that occurs in the absence of actomyosin flows, and another (at about 50% egg length) that occurs with actomyosin flows [35]. We show that the first boundary position can be obtained by propagating a local zone of PAR-3 depletion in the presence of mutual inhibition with pPARs. The second case suggests that flows alter the flux balance between the anterior and posterior domains, thus shifting the boundary positions. Indeed, there is a steady state nonzero flow profile observed during maintenance phase, corresponding to an asymmetry in myosin intensity across the A/P boundary [30].

Two questions arise when we consider this data: first, how is the myosin asymmetry maintained without cues? Second, what “brakes” the contractility, i.e., what stops the anterior cap from contracting off the end of the embryo? The first question can be answered again through

experiments and modeling, which have shown that PAR proteins feedback onto myosin dynamics [14, 1]. It remains unclear whether this occurs through pPARs inhibiting myosin (as suggested by [1]) or aPARs recruiting myosin (or inhibiting its dissociation, as suggested in [14]). Modeling work has shown that pPARs *must* inhibit myosin to propagate initially asymmetric protein distributions [20]. Seeing as this hypothesis has been supported experimentally [27, 1], it is the one we use in this work.

Once we set up dynamics in which aPARs and pPARs are mutually bistable, and pPARs inhibit myosin, it is straightforward to see how maintenance phase “rescue” could occur, as the already expanding pPAR domain is then further extended by flow caused from inhibited myosin. But how could this process stop? Previous work [12] proposes a “pinning” of the boundary [26] based on cytoplasmic depletion of PAR-2. As the PAR-2 domain expands, the amount available in the cytoplasm decreases. This changes the local binding/unbinding equilibrium, leading to relative depletion of PAR-2 in the posterior. This levels off myosin inhibition levels, which prevents the build up of strong flows, stalling the boundary.

We propose that this mechanism, while theoretically possible and reproducible in our model, is not the one primarily responsible for stalling the boundary movement. Instead, we postulate that branched actin acts to inhibit contractility in the anterior domain, which prevents myosin from building up and generating stronger flows. We demonstrate **one of these two things**:

1. The hypercontractile state is stable. We can pin it down with the PAR-2 wave-pinning mechanism. The model predicts decreasing PAR-2 on the posterior in this case, which is supported by our experiments.
2. The hypercontractile state is not stable. While we can reproduce it in the model, there is no way to reconcile the parameters we need to reproduce it with the parameters we need to reproduce the wild-type.

Finally, we use modeling to show that branched actin-mediated inhibition of myosin leads to the experimentally-observed myosin and flow profiles, thus validating our hypothesis.

## 2 Dynamics of myosin in the embryo

We begin by considering a model of myosin by itself, to determine if it can spontaneously polarize. Spontaneous polarization of myosin, if possible, would explain the maintenance-phase rescue

experiments that we observe.

## 2.1 Myosin as a self-patterning material

Let us begin by building a toy model for myosin dynamics. This section is a summary of the paper [2], which considers the same problem. The novelty in what we do will come later, when we couple myosin to branched actin and other proteins.

We describe the dynamics of myosin  $M(x, t)$  using the advection-diffusion equation

$$\partial_t M + \partial_x (vM) = D_M \partial_x^2 M. \quad (1)$$

The complication is that the myosin is advected through a velocity field of its own making. The velocity field comes from stress generated in the fluid,

$$\sigma = \eta \partial_x v + \sigma_a(M), \quad (2)$$

which is a combination of viscous stress and active stress. As in [2], we ignore the elastic part of the stress, assuming the actomyosin cortex is purely viscous when in reality it is visco-elastic. The force balance equation in the fluid says that the force due to stress must be balanced by the drag force,

$$\gamma v = \partial_x \sigma, \quad (3)$$

where  $\gamma$  is the drag coefficient. Combining the force balance (3) with the stress expression (2) gives an auxillary equation for the velocity field

$$\gamma v = \eta \partial_x^2 v + \partial_x \sigma_a(M) \quad (4)$$

which couples to the myosin equation (1) via the active stress.

The advection-diffusion equation (1) is mass-preserving, meaning that the uniform steady state is just given by  $M_0 = \frac{1}{L} \int_0^L M(x, 0) dx$ . For the active stress, we let  $\sigma_a = \sigma_0 \hat{\sigma}_a(M)$ . The analysis of [2] shows that (for periodic boundary conditions) the uniform steady state is unstable when

$$\text{Pe} \times \frac{M_0 (\partial_M \hat{\sigma}_a (M_0))}{1 + (2\pi\ell/L)^2} > 1, \quad (5)$$

where  $\ell = \sqrt{\eta/\gamma}$  is the characteristic lengthscale over which velocity decays (the diffusive lengthscale for velocity),  $L$  is the system length, and the Peclet number

$$\text{Pe} = \frac{\sigma_0}{D_M \gamma} \quad (6)$$

Parameter	Description	Value	Units	Ref	Notes
$L$	Domain length	134.6	$\mu\text{m}$	[12]	radii $27 \times 15 \mu\text{m}$ ellipse
$h$	Cytoplasmic “thickness”	9.5	$\mu\text{m}$	[12]	(area/circumference)
$D_M$	Myosin diffusivity	0.05	$\mu\text{m}^2/\text{s}$	[14]	
$k_M^{\text{on}}$	Myosin attachment rate	0.5	$\mu\text{m}/\text{s}$		Fit to get 30% bound myosin
$k_M^{\text{off}}$	Myosin detachment rate	0.12	1/s	[14]	
$M^{(\text{Tot})}$	Maximum bound myosin density	–	#/ $\mu\text{m}$		Scales out of equations
$\eta$	Cytoskeletal fluid viscosity	0.1	$\text{Pa}\cdot\text{s}$		$100 \times$ water
$\gamma$	Myosin drag coefficient	$10^{-3}$	$\text{Pa}\cdot\text{s}/\mu\text{m}^2$		$\ell = \sqrt{\eta/\gamma} = 10 \mu\text{m}$ [29]
$\sigma_0$	Stress coefficient and form	0.0042	Pa		Fit in Sec. 2.2.2
$\hat{\sigma}_a(\hat{M})$	Stress function of myosin	$\hat{M}$			Fit in Sec. 2.2.2

**Table 1:** Parameter values for myosin model. All of these parameters listed with a citation are lifted directly from the corresponding paper. Remaining parameters: the on rate  $k_M^{\text{on}}$  is chosen to give 30% bound myosin [14, Fig. S3]. Later this rate will change in the presence of CDC-42. We make an assumption about the fluid viscosity  $\eta$ , which then gives us the drag coefficient  $\gamma$  from  $\ell = 10 \mu\text{m}$  [14]. The remaining parameters are fit in Section 2.2.2 from the wild-type data of [30].

expresses the ratio of advective transport to diffusive transport. Qualitatively, the system has a uniform steady state and a second peaked steady state, where advective flux into the peaks matches the diffusive flux into the peaks. For this steady state to be stable, the advective transport must be sufficiently large relative to diffusive transport, so the Peclet number must be sufficiently large.

## 2.2 Myosin pattern formation with turnover

We now introduce a single species model of myosin with turnover,

$$\partial_t M + \partial_x(vM) = D_M \partial_x^2 M + k_M^{\text{on}} M_{\text{cyto}} - k_M^{\text{off}} M \quad (7a)$$

$$\gamma v = \eta \partial_x^2 v + \partial_x \sigma_a(M) \quad (7b)$$

$$M_{\text{cyto}} = \frac{1}{hL} \left( M^{(\text{Tot})} L - \int_0^L M(x) dx \right) \quad (7c)$$

It will be useful to nondimensionalize this equation, using the scalings

$$x = \hat{x}L \quad t = \hat{t}/k_M^{\text{off}} \quad M = \hat{M}M^{(\text{Tot})} \quad v = \hat{v} \frac{\sigma_0}{\sqrt{\eta\gamma}} \quad (8)$$

The resulting equations are

$$\partial_{\hat{t}} \hat{M} + \hat{\sigma}_0 \partial_{\hat{x}} (\hat{v} \hat{M}) = \hat{D}_M \partial_{\hat{x}}^2 \hat{M} + \hat{K}_M^{\text{on}} \left( 1 - \int_0^1 \hat{M}(x) dx \right) - \hat{M} \quad (9a)$$

$$\hat{v} = \hat{\ell}^2 \partial_{\hat{x}}^2 v + \hat{\ell} \partial_{\hat{x}} \hat{\sigma}_a(\hat{M}) \quad (9b)$$

and are controlled by the dimensionless parameters

$$\hat{\sigma}_0 = \left( \frac{\sigma_0 / \sqrt{\eta\gamma}}{L k_M^{\text{off}}} \right) \quad \hat{D}_M = \frac{D_M}{k_M^{\text{off}} L^2} \quad \hat{K}_M^{\text{on}} = \frac{k_M^{\text{on}}}{h k_M^{\text{off}}} \quad \hat{\ell} = \frac{\sqrt{\eta/\gamma}}{L}. \quad (10)$$

Recalling that  $1/k_M^{\text{off}}$  is the residence time, these dimensionless parameters can be understood in the following way:

1.  $\hat{\sigma}_0$  is the fraction of the domain that active transport occurs on before a myosin molecule jumps off. To see this, note that residence time  $\times$  the advective velocity  $\sigma_0 / \sqrt{\eta\gamma}$  is the amount of motion, which is normalized by the domain length.
2.  $\hat{D}_M$  is the maximum fraction of the domain a molecule diffuses before it unbinds (in the extreme case when the gradient in the domain is  $1/L$ , the diffusive velocity is  $D_M/L$ ).
3.  $\hat{K}_M^{\text{on}}$  is the ratio of the binding rate to unbinding rate when all the molecules are cytoplasmic. The uniform steady state of the model is given by  $\hat{M}_0 = \hat{K}_M^{\text{on}} / (1 + \hat{K}_M^{\text{on}})$ .
4.  $\hat{\ell}$  is the ratio of the hydrodynamic lengthscale to the domain length.

Prior to performing linear stability analysis, we need to first determine the function  $\sigma_a$  and the other parameters. We do this in the next section by fitting experimental data.

### 2.2.1 Parameter estimation

Table 1 lists the parameters for the myosin model. According to [12], the *C. elegans* embryo has a roughly ellipsoidal shape, with half-axis lengths  $27 \times 15 \times 15 \mu\text{m}$ . As such, our model will be a  $27 \times 15$  ellipse, which has perimeter  $L = 134.6 \mu\text{m}$ . In our one-dimensional model, the cytoplasm has a “thickness” which is just the area of the ellipse  $1272 \mu\text{m}^2$  divided by the perimeter  $L$ , which gives  $h = 9.5 \mu\text{m}$ .

The next category of parameters relates to the myosin kinetics. The in-membrane diffusivity of myosin, as well as the detachment rate, have both been measured in [14]. For the attachment rate, it was estimated in [14, Fig. S3m] that roughly 30% of myosin is bound to the cortex in wild-type

embryos. Recalling that the uniform steady state is  $\hat{M}_0 = \hat{K}_M^{\text{on}} / (1 + \hat{K}_M^{\text{on}})$ , this gives  $\hat{K}_M^{\text{on}} = 0.43$ , or  $k_M^{\text{on}} = 0.43 h k_M^{\text{off}} = 0.5 \mu\text{m/s}$ . The last parameter, the total amount of myosin, scales out of the equations. This is fortunate for us because it is difficult to think about a total amount over a cross-section.

For the fluid parameters, we assume that the viscosity of the cytoskeletal fluid on the cortex is 100 times water, which gives 0.1 Pa·s. The “hydrodynamic length scale” of  $\ell = \sqrt{\eta/\gamma} = 10 \mu\text{m}$ , measured in [29], then gives the myosin drag coefficient  $\gamma$ . But more important than either of these is the stress as a function of myosin concentration. We fit this from the wild-type data of [30] in the next section.

### 2.2.2 Inferring flow profile from experiments

Because we can measure the cortical velocity and myosin intensity, we can actually infer the function  $\sigma_a(M)$  in dimensional units from the experimental data [30]. We in particular isolate the myosin intensity and flow speed during “late maintenance” phase in wild type embryos [30, Fig. 1B(bottom)], plotting the results in the top panels of Fig. 1. In the top left plot, we plot the myosin intensity, normalized so that the mean amount of bound myosin is 0.3, in accordance with wild-type measurements in [14, Fig. S3].

In the top right plot, we show the velocity in  $\mu\text{m}/\text{min}$ . In both cases, the data are plotted on  $\hat{x} \in [0.25, 0.75]$ , which corresponds to half of the embryo (one of the lines going from anterior to posterior end). We then periodically extend this data so that we fill the whole circumference  $\hat{x} \in [0, 1]$ ; these are the blue lines in Fig. 1. Finally, to remove the noise from our measurements (e.g., the strange dips in the myosin concentration at the anteior and posterior pole), we fit the periodized version with a two-term (+constant) Fourier representation, which gives the red lines in Fig. 1.

To extract the stress profile from the smoothed velocity and myosin intensity, we consider a hybrid dimensional form of (7b)

$$\gamma v - \frac{\eta}{L^2} \partial_{\hat{x}}^2 v = \frac{1}{L} \partial_{\hat{x}} \sigma_a(M).$$

Let the Fourier series representation for  $v(\hat{x}) = \sum_k \tilde{v}(k) \exp(2\pi i k \hat{x})$ , and likewise for  $\hat{\sigma}_a$ . Then, in Fourier space, the solution for  $\sigma_a$  is given by

$$\sigma_a(k) = \frac{\gamma + \eta/L^2 (2\pi k)^2}{2\pi i k/L} \tilde{v}(k). \quad (11)$$

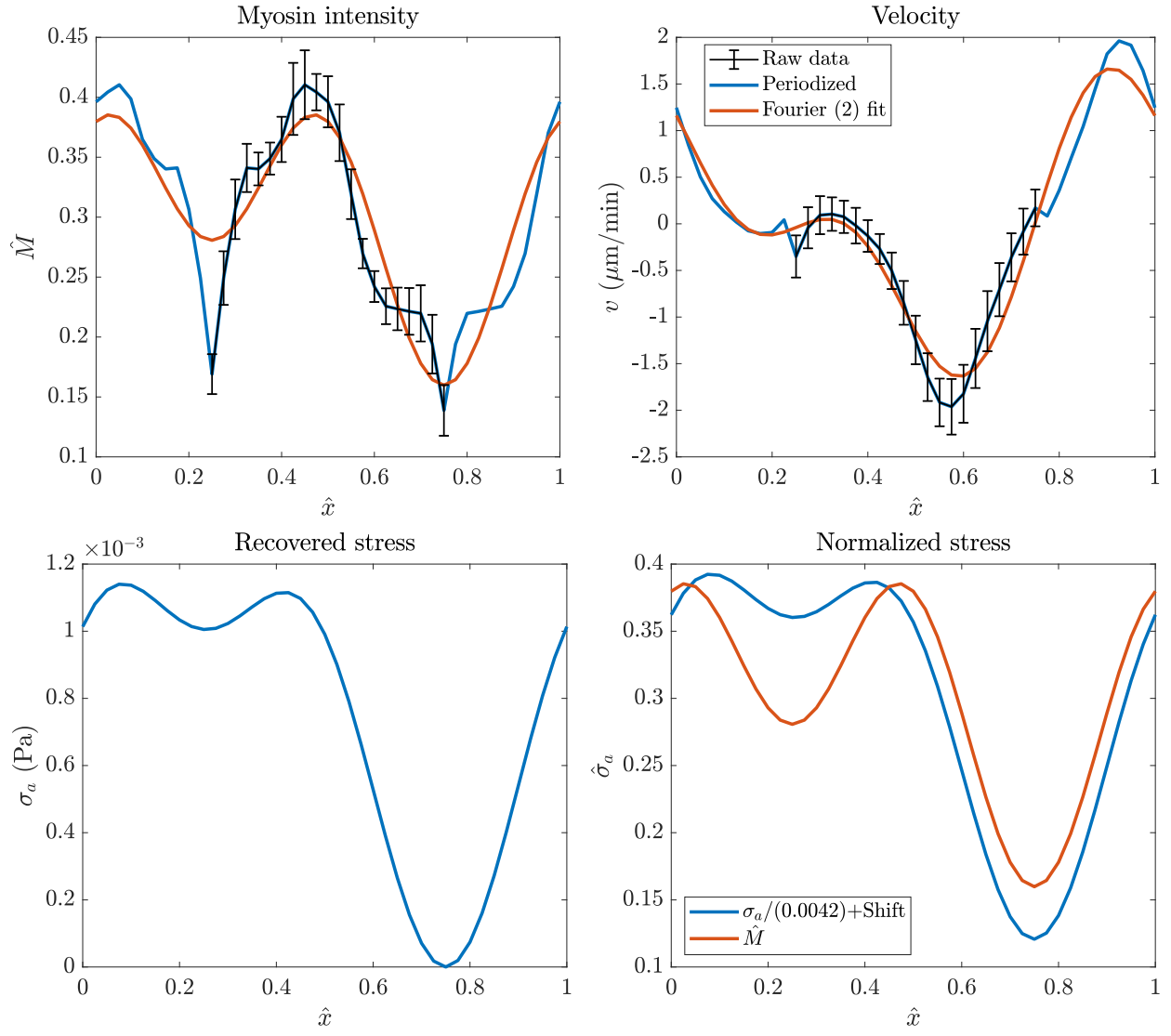


**Figure 1:** Extracting the velocity profile and active stress from wild-type embryos. Top: the experimental data for myosin intensity (left) and velocity in  $\mu\text{m}/\text{min}$  (right). We show the raw data in black (which goes from anterior to posterior), the periodized version in blue, and a two-term (three terms if we include the constant) Fourier series representation in red. Bottom left: the recovered stress profile  $\sigma_a(\hat{x})$  in dimensional units. Bottom right: comparing the recovered stress to the myosin intensity, after normalizing by  $\sigma_0 = 0.0011$  Pa. It is clear that  $\hat{\sigma}_a = \hat{M}$  is a reasonable approximation.

The  $k = 0$  mode is undefined because  $\sigma_a$  only appears differentiated; we therefore set it such that the real space stress has a minimum value of zero.

We plug the parameters from Table 1 into (11) and show the resulting real space stress in the bottom left panel of Fig. 1. This is the dimensional stress  $\sigma_a$ . In the right panel of Fig. 1, we normalize and shift the stress so that it has the same mean and range as the myosin profile  $\hat{M}$ . Obtaining the same range allows us to read off the constant  $\sigma_0 = 4.2 \times 10^{-3}$  Pa that controls the magnitude of the advective flows. In particular, the dimensionless parameter  $\hat{\sigma}_0$  defined in (10) is seen to be equal to

$$\hat{\sigma}_0 = \left( \frac{\sigma_0 / \sqrt{\eta\gamma}}{Lk_M^{\text{off}}} \right) = 0.026. \quad (12)$$

In addition, the bottom right panel of Fig. 1, also shows that we can roughly set

$$\hat{\sigma}_a = \hat{M} \quad (13)$$

as a good approximation to the stress. The function itself is ambiguous, since  $\hat{M} = 0.3$  defines two different values of the stress depending on the side of the domain, but  $\hat{\sigma}_a = \hat{M}$  appears to be a good approximation.

We confirm this in Fig. 2, where we repeat the velocity fitting procedure in *arx-2* (RNAi) embryos, which lack branched actin and consequently have a simpler velocity profile. To compute the myosin profile, we assume that the experimentally-measured intensity can be converted to the dimensionless concentration  $\hat{M}$  via the same factor (0.21) as wild-type embryos. Consequently, the myosin profile we obtain is in the top left of Fig. 2. The velocity is shown in the top right panel, and we extract the stress profile in the bottom left in exactly the same way as in wild-type. Then, to compute normalized stress we divide out by  $\hat{\sigma}_0 = 4.2 \times 10^{-3}$  Pa (obtained from wild-type). The normalized stress, when shifted by an arbitrary constant, lines up almost perfectly with the smoothed myosin profile, demonstrating that our rough approach from wild-type embryos extends to other embryos as well. Thus, this section gives us  $\sigma_a = (4.2 \times 10^{-3}) \hat{M}$ .

### 2.2.3 Linear stability analysis

Now that all the parameters are known, we can perform linear stability analysis to see if the system could spontaneously polarize. The uniform steady state is  $\hat{M}_0 = \hat{K}_M^{\text{on}} / (1 + \hat{K}_M^{\text{on}})$ . We consider a perturbation around that state  $\hat{M} = \hat{M}_0 + \delta\hat{M}$ , where  $\delta\hat{M} = \delta\hat{M}_0 e^{\lambda(k)\hat{t} + 2\pi i k \hat{x}}$ . Plugging this into

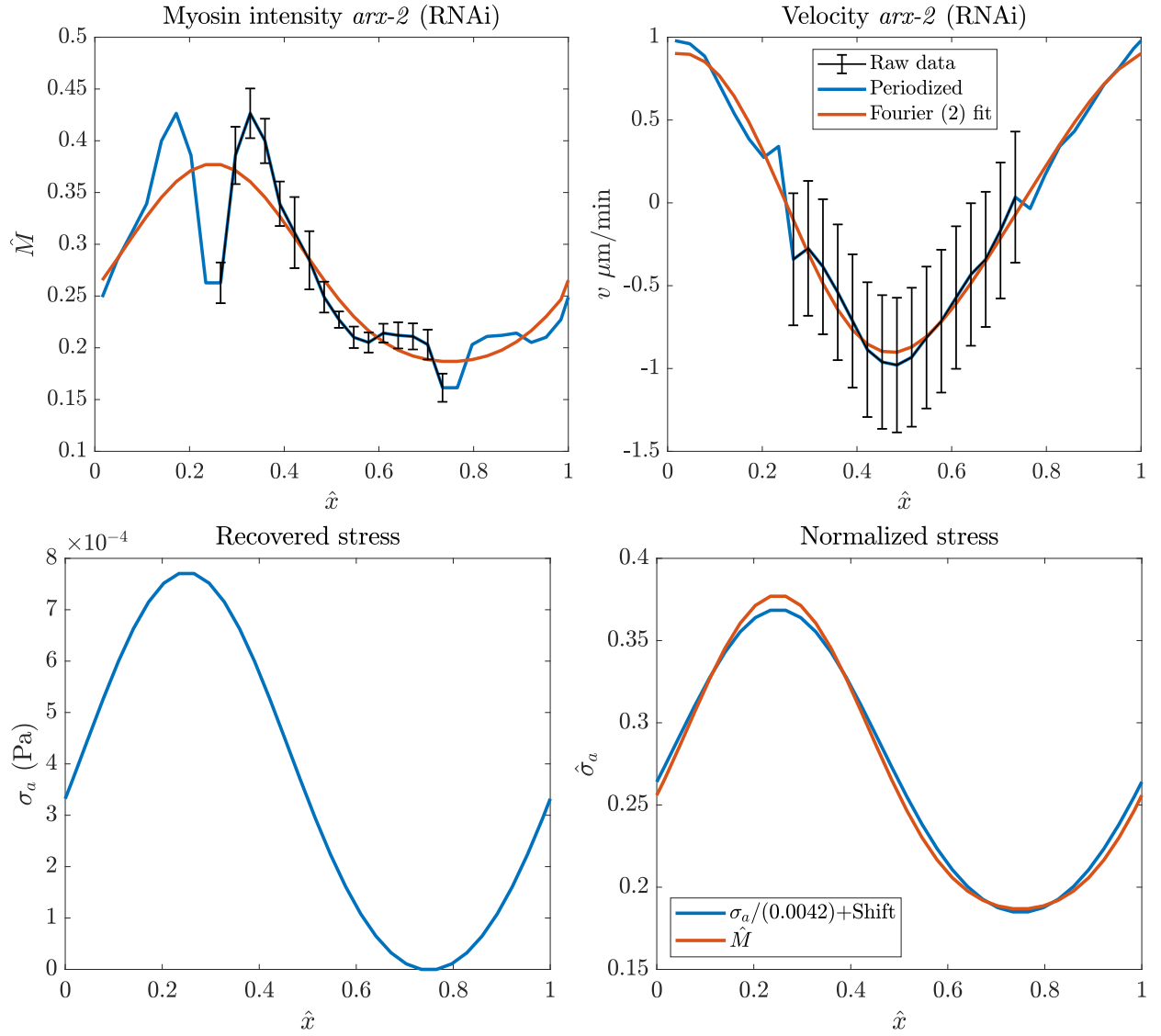


**Figure 2:** Same plot as Fig. 1, but in  $arx-2$  (RNAi) embryos. In the bottom right plot, we normalize by  $\sigma_0 = 1.1 \times 10^{-3}$  Pa. This makes the stress (when shifted by an arbitrary constant) roughly the same as the myosin profile (also normalized so its maximum is 1).

(9b), we get the velocity [2, Eq. (11)]

$$\hat{v} = \frac{2\pi i k \hat{\ell} \hat{\sigma}'_a(\hat{M}_0)}{1 + (2\pi k \hat{\ell})^2} \hat{\delta} M. \quad (14)$$

Substituting this velocity into (9a), and considering only the first order terms, we get the following equation for the eigenvalues

$$\lambda(k) = \frac{4\pi^2 k^2 \hat{\ell} \hat{M}_0 \hat{\sigma}_0 \hat{\sigma}'_a(\hat{M}_0)}{1 + 4\pi^2 k^2 \hat{\ell}^2} - \hat{D}_M 4\pi^2 k^2 - 1 \quad (15)$$

Using the parameters we have obtained, we have the following values for the dimensionless groups

$$\hat{D}_M = 2.3 \times 10^{-5} \quad \hat{M}_0 \approx 0.3 \quad \hat{\sigma}'_a = 1 \quad \hat{\ell} \approx 0.07 \quad (16)$$

This gives the dispersion relation shown in Fig. 3 for different values of  $\hat{\sigma}_0$ . We observe strong flow coupling required for instability; with  $\hat{\sigma}_0 = 0.2$  (flow transports myosins around 20% of the cell before they come off), we still do not see any instability. Considering that we already have seen wild-type embryos have  $\sigma_0 \approx 0.004$ , it is clear that myosin cannot self-polarize in the zygote.

Importantly, the large value of  $\sigma_0$  needed for instability is a consequence of the  $-1$  in the dispersion relation (15), which comes from the unbinding kinetics. Thus, unbinding makes it *harder* to destabilize the uniform steady state. Indeed, without the  $-1$ , the instability occurs at  $\hat{\sigma}_0 \approx 10^{-3}$ , which is pretty weak coupling to the flow. When we account for unbinding, diffusion becomes so small as to be irrelevant, as for the  $k = 1$  mode the coefficient in (15) is  $\hat{D}_M 4\pi^2 \approx 10^{-3}$ . **Thus, the real balance here (to generate the instability) is not between advection and diffusion, but between advection and unbinding.** Specifically, the advective flow must be strong enough to overcome the increase in unbinding that happens in areas enriched in myosin.

### 3 PAR-3 as the anchor for asymmetries

We are motivated first by the experimental observations that asymmetries in the PAR proteins are stable once set up, even in the absence of contractility. This experimental observation tells us that there is an intrinsic bistability in the biochemical circuit, which switches from a uniform state to a polarized state. In later sections, the switch will occur under the influence of actomyosin flows, while in this section the initial conditions will be the only way to switch the steady profiles.

Unlike in budding yeast cells [25], there is no experimental evidence that *C. elegans* cells can spontaneously polarize, which means that the system is truly bistable. Traditionally, it has been

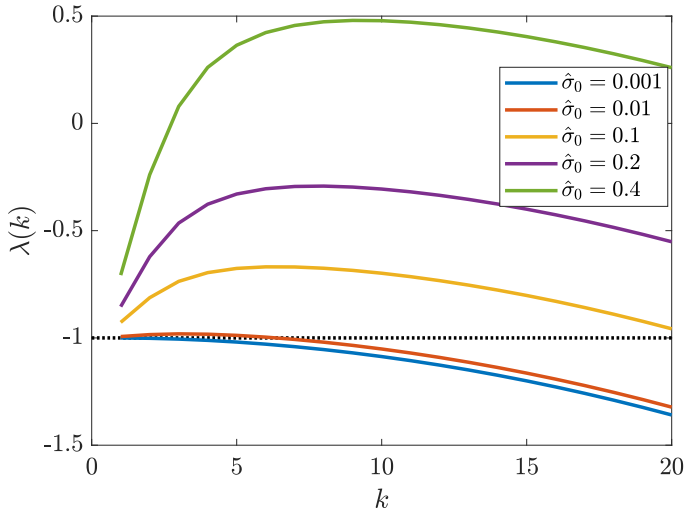


**Figure 3:** Dispersion relation (15) for myosin for different values of  $\hat{\sigma}_0$ . Positive eigenvalues indicate instability of the steady state. Dotted black line at  $\lambda = -1$  reflects the axis of instability *without* unbinding kinetics.

speculated that the bistability comes from mutual inhibition of the aPAR and pPAR proteins [15, 33]. But translating this idea into equations becomes much harder than might be expected! Indeed, ODEs based on first-order mass action kinetics of aPAR-pPAR inhibition *do not* yield bistable dynamics under any choice of parameters [5]. Attempts to overcome this have used stoichiometric coefficients for the biochemical equations that guarantee bistability [12, 14] or included actomyosin flows designed to transport the aPARs [32]. Both of these approaches are grounded more in intuition than in biological evidence, as there is no reason to doubt mass action kinetics, and recent experiments have shown that both aPARs and pPARs are transported by myosin [18].

Recent experimental observations about PAR-3 provide a potential way out of this conundrum. Indeed, it was recently shown that PAR-3 asymmetries are stable even in the absence of its posterior inhibitor PAR-1, which suggest that the dynamics of PAR-3 *by itself* are intrinsically bistable [21]. Experimental evidence has shown that the bistability occurs via a mechanism in which membrane-bound PAR-3 recruits additional cytoplasmic monomers to the membrane. One goal of this section is to translate these observations into equations which demonstrate how PAR-3 can set up and maintain an asymmetry in the absence of posterior inhibition. We then incorporate posterior PAR proteins and show how their inclusion modifies the dynamics of PAR-3, potentially shifting the boundary between the two protein domains.

### 3.1 Basic equations and framework for PAR-3

We first formulate our model of PAR-3 dynamics, which is based on that of Lang and Munro [23]. The key property of PAR-3 that makes it different from other proteins is its ability to form *oligomers* on the membrane. Unlike monomers, these oligomers do not diffuse in the membrane, and are not found in high concentrations in the cytoplasm. Based on these experimental observations, we will consider a model in which there are two species of PAR-3,

1. Monomeric PAR-3, which can be found in cytoplasmic form ( $A_{\text{cyto}}$ ) or membrane bound ( $A_1$ ) form, and can diffuse on the membrane.
2. Oligomerized PAR-3 ( $A_n$ ) which is only found on the membrane, and cannot diffuse there.

We will let the number of oligomers of size  $n$  be denoted by  $A_n$ .

Given these assumptions, the model equations in dimensional form are as follows

$$\partial_t A_1 = D_A \partial_x^2 A_1 + (k_A^{\text{on}} + k_A^+ f_A^+ (A_1, A_n)) A_{\text{cyto}} + 2k_A^{\text{dp}} A_n - 2k_A^p A_1^2 - k_{A,1}^{\text{off}} A_1 \quad (17a)$$

$$\partial_t A_n = k_A^p A_1 A_{n-1} - k_A^{\text{dp}} A_n - k_{A,n}^{\text{off}} A_n \quad n \geq 2 \quad (17b)$$

$$A_{\text{cyto}} = \frac{1}{hL} \left( A^{(\text{Tot})} L - \int_0^L A(x) dx \right) \quad A(x) = \sum_{n=1}^N n A_n(x) \quad (17c)$$

A complete list of parameters with units and values is given in Table 2, but it will be helpful to point out the important ones in our model. First, the feedback strength  $k_A^+$ , which has units of length<sup>2</sup>/time, gives the rate at which cytoplasmic PAR-3 is recruited to the membrane. It is multiplied by the flux function  $f_A^+$ , which gives the strength of recruitment (in units of inverse length). The overall on rate is proportional to the cytoplasmic concentration, which is defined in (17c). There  $A^{(\text{Tot})}$  expresses the density of bound PAR-3 when all molecules are bound to the membrane (units 1/length). Subtracting the amount of bound PAR-3 and dividing by the membrane area gives the cytoplasmic concentration in units of 1/area.

### 3.2 Dimensionless form

A sensible timescale for the system is the time a given PAR-3 molecule spends on the membrane. Because about 80% of the bound PAR-3 molecules are in oligomer form, and since the depolymerization reaction is much slower than the unbinding reaction, we nondimensionalize time by  $1/k_A^{\text{dp}}$ . This gives the dimensionless (hatted) variables defined by

$$x = \hat{x}L \quad t = \hat{t}/k_A^{\text{dp}} \quad A = \hat{A} A^{(\text{Tot})}.$$

Substituting into (17) gives the rewritten dynamics

$$\begin{aligned}\partial_{\hat{t}} \hat{A}_1 &= \hat{D}_A \partial_{\hat{x}}^2 A_1 + \hat{K}_A^{\text{on}} \left( 1 + \hat{K}_A^{\text{f}} \hat{F}_A^+(\hat{A}_1, \hat{A}_n) \right) \left( 1 - \int_0^1 \hat{A}(x) d\hat{x} \right) \\ &\quad + 2\hat{A}_n - 2\hat{K}_A^{\text{p}} \hat{A}_1^2 - \hat{K}_{A,1}^{\text{off}} \hat{A}_1\end{aligned}\tag{18a}$$

$$\partial_{\hat{t}} \hat{A}_n = \hat{K}_A^{\text{p}} \hat{A}_1 \hat{A}_{n-1} - \hat{A}_n - \hat{K}_{A,n}^{\text{off}} \hat{A}_n \quad n \geq 2\tag{18b}$$

$$\begin{aligned}\hat{D}_A &= \frac{D_A}{L^2 k_A^{\text{dp}}}, \quad \hat{K}_A^{\text{on}} = \frac{k_A^{\text{on}}}{k_A^{\text{dp}} h}, \quad \hat{K}_A^{\text{f}} = \frac{k_A^+ A^{(\text{Tot})}}{k_A^{\text{on}}}, \quad \hat{K}_{A,n}^{\text{off}} = \frac{k_{A,n}^{\text{off}}}{k_A^{\text{dp}}}, \\ \hat{K}_A^{\text{p}} &= \frac{k_A^{\text{p}} A^{(\text{Tot})}}{k_A^{\text{dp}}}, \quad \hat{F}_A^+(\hat{A}_1, \hat{A}_n) = \frac{f_A^+(\hat{A}_1, \hat{A}_n)}{A^{(\text{Tot})}}\end{aligned}\tag{18c}$$

and we have used the convenient shorthand  $A = \sum n A_n$  and likewise for the hatted variables.

### 3.3 Quasi-steady state approximation

We make the quasi-steady state approximation [23] that the oligomerization kinetics are in equilibrium relative to the other processes. This means that the distribution of oligomer sizes is exponential [8, 23]

$$\hat{A}_n = \hat{K}_A^{\text{p}} \hat{A}_1 \hat{A}_{n-1} := \alpha \hat{A}_{n-1} \quad n \geq 2.\tag{19}$$

This defines  $\alpha = \hat{K}_A^{\text{p}} \hat{A}_1$  as the coefficient of the exponential distribution of oligomer sizes. It follows that the total number of monomers is given by

$$\hat{A} = \sum_{n=1}^N n \alpha^{n-1} \hat{A}_1 \rightarrow \frac{\hat{A}_1}{(1-\alpha)^2}.\tag{20}$$

This equation can then be solved for  $\hat{A}_1$  to obtain [23, Eq. (12)]

$$\hat{A}_1 = \frac{1 + 2\hat{A} \hat{K}_A^{\text{p}} - \sqrt{1 + 4\hat{K}_A^{\text{p}} \hat{A}}}{2\hat{A} \left( \hat{K}_A^{\text{p}} \right)^2},\tag{21}$$

which gives the number of bound monomers as a function of the total bound  $\hat{A}$ .

The quasi-steady state approximation reduces the dynamics (18) to a single equation for  $\hat{A} = \sum n \hat{A}_n$ , obtained by summing (18a) and (18b) and invoking (19)

$$\partial_{\hat{t}} \hat{A} = \hat{D}_A \partial_{\hat{x}}^2 A_1 + \hat{K}_A^{\text{on}} \left( 1 + \hat{K}_A^{\text{f}} \hat{F}_A^+(\hat{A}) \right) \left( 1 - \int_0^1 \hat{A}(x) d\hat{x} \right) - \sum_{n=1}^{\infty} n \hat{K}_{A,n}^{\text{off}} \alpha^{n-1} \hat{A}_1.\tag{22}$$

We will consider two cases for the off-rate: in the first case, we assume that only monomers can unbind, which gives [21, Eq. (14)]

$$\partial_{\hat{t}} \hat{A} = \hat{D}_A \partial_{\hat{x}}^2 A_1 + \hat{K}_A^{\text{on}} \left( 1 + \hat{K}_A^{\text{f}} \hat{F}_A^+(\hat{A}) \right) \left( 1 - \int_0^1 \hat{A}(x) d\hat{x} \right) - \hat{K}_{A,1}^{\text{off}} \hat{A}_1.\tag{23}$$

In the second case, we use the experimentally-fit curve  $\hat{K}_{A,n}^{\text{off}} = \hat{K}_{A,1}^{\text{off}} \beta^{n-1}$ , which gives

$$\begin{aligned} \sum_{n=1}^{\infty} n \hat{K}_{A,n}^{\text{off}} \alpha^{n-1} \hat{A}_1 &= \hat{K}_{A,1}^{\text{off}} \hat{A}_1 \sum_{n=1}^{\infty} n (\beta \alpha)^{n-1} = \frac{k_{A,1}^{\text{off}} \hat{A}_1}{(1 - \beta \alpha)^2} \\ \partial_t \hat{A} &= \hat{D}_A \partial_x^2 \hat{A}_1 + \hat{K}_A^{\text{on}} \left( 1 + \hat{K}_A^{\text{f}} \hat{F}_A^+(\hat{A}) \right) \left( 1 - \int_0^1 \hat{A}(x) d\hat{x} \right) - \hat{K}_{A,1}^{\text{off}} \frac{\hat{A}_1}{\left( 1 - \beta \hat{K}_A^{\text{p}} \hat{A}_1 \right)^2} \end{aligned} \quad (24)$$

Seeing as setting  $\beta = 0$  in (24) gives (23), we can see that (24) is the most general single-species equation that we can write. This is the equation we will solve going forward.

### 3.4 Parameters

Recent experimental measurements [21] give accurate measurements for three of the parameters: the diffusion coefficient  $D_A = 0.1 \mu\text{m}^2/\text{s}$ , the detachment rate  $k_{A,n}^{\text{off}} = 3\beta^{n-1}$  with  $\beta = 0.25$ , and the depolymerization rate  $k_A^{\text{dp}} = 0.08/\text{s}$ . The values of these parameters are summarized in Table 2, and determine the dimensionless parameters  $\hat{D}_A$  and  $\hat{K}_A^{\text{off}}$ . We determine  $\hat{K}_A^{\text{on}}$ ,  $\hat{K}_A^{\text{p}}$ ,  $\hat{K}_A^{\text{f}}$ , and the form of the feedback function via a systematic fitting procedure as detailed next.

#### 3.4.1 Fitting the polymerization rate

The first parameter we need to fit the polymerization rate is the percentage of PAR-3 bound to the membrane in the uniform state. The uniform state can be realized by considering mutants which lack a functional sperm cue and thus do not polarize [21, Fig. S1]. These mutants show a peak PAR-3 concentration in late interphase; late maintenance phase then gives a bound concentration that is roughly 50% of this peak. We will assume that almost all of the PAR-3 is bound in late interphase, so that the uniform state in late maintenance is at  $\hat{A}_u := \hat{A}_1 + 2\hat{A}_n \approx 0.5$ . The observation that these embryos do not polarize implies that the uniform state is stable, and the estimate for the percentage of bound protein is similar to that obtained for PAR-2 at the end of maintenance phase in [14, Fig. S3].

When there is no posterior inhibitor, the concentration of bound PAR-3 during late maintenance phase in the anterior is roughly  $\hat{A}_a = 1.2u \approx 0.6$  (this comes from comparing fluorescence in PAR-1 mutant and spd-5 mutant embryos shown in Figs. 2 and S1 of [21]). In PAR-1 mutants, the concentration in the posterior is then roughly 10% of the anterior, or  $\hat{A}_p = 0.06$ .

These measurements allow us firstly to determine the relative polymerization rate  $\hat{K}_A^{\text{p}}$ . The distribution of oligomer sizes in PAR-1 mutant embryos was measured in [21] on both the anterior

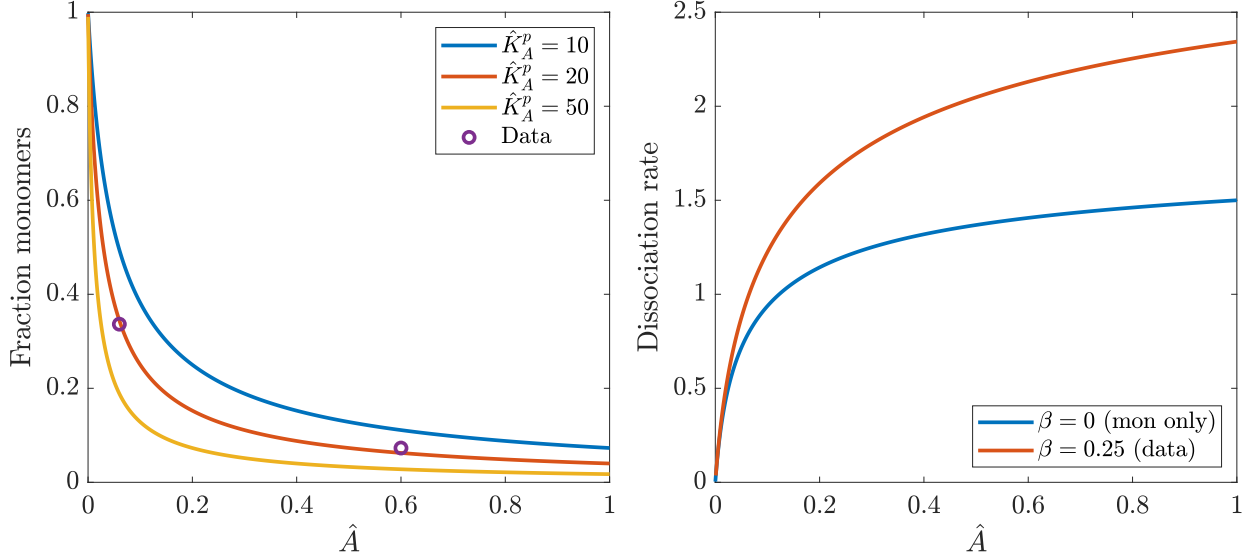


**Figure 4:** Comparing polymerization dynamics with different panels. Left panel: the fraction of monomers as a function of bound  $\hat{A}$  with three different values of  $\hat{K}_A^p$ . The polymerization rate  $\hat{K}_A^p = 20$  best fits the data. Right panel: the effective dissociation rate as a function of  $\hat{A}$  with two different assumptions: only monomers can dissociate (blue curve), and dissociation occurs with the experimentally determined rate  $k_{A,n}^{\text{off}} = k_{A,1}^{\text{off}} \beta^{n-1}$  for  $\beta = 0.25$  (red curve).

and posterior side. There it was shown that the distribution is roughly exponential, with  $\alpha = 0.42$  on the posterior side (30% in monomer form), and  $\alpha = 0.73$  on the anterior side (10% in monomer form). When we substitute  $\hat{K}_A^p = 20$  into (21), we obtain  $\alpha(\hat{A} = 0.06) = 0.41$  and  $\alpha(\hat{A} = 0.6) = 0.75$ . This is shown in the left panel of Fig. 4.

### 3.4.2 The dissociation rate

The formula for the number of monomers (21) shows that, as  $\hat{A}$  increases, we expect to get a constant number of monomers on the membrane. If we only consider dissociation of monomers, then we expect the dissociation rate to be a constant as  $\hat{A}$  increases, which can render the steady state extremely sensitive to changes in  $\hat{A}$  (if the attachment rate shifts upwards slightly,  $\hat{A}$  has to increase by a lot for the detachment rate to compensate). This behavior is shown in the right panel of Fig. 4. There we see that the dissociation rate

$$\hat{K}_{A,1}^{\text{off}} \frac{\hat{A}_1}{\left(1 - \beta \hat{K}_A^p \hat{A}_1\right)^2} \quad (25)$$

is roughly constant as  $\hat{A}$  increases when  $\beta = 0$ , and only monomers unbind. When we use the experimental profile with  $\beta = 0.25$ , we see a curve with a larger slope at  $\hat{A} = 1$ . This is the curve we will consider going forward.

### 3.4.3 The form of the feedback strength – linear feedback models

Before we get into fitting the feedback parameters, it is important to consider the nature of the feedback model. Our model is based strongly on that of Lang and Munro [23], who used the linear feedback model  $f_A^+(A) = A$ . To analyze the characteristics of this model, we consider two representative examples in Fig. 5, where we look at the attachment and detachment fluxes as a function of  $\hat{A}$ . The detachment flux is simply (25), and is therefore set by the red line. The attachment flux varies depending on the model considered. If we consider a uniform state, then the cytoplasmic concentration is simply  $1 - \hat{A}$ , and there is a single uniform steady state (intersection of dotted blue and red lines). In polarized states, the concentration is not necessarily uniform, and so we analyze the stability of the steady state by taking the cytoplasmic concentration as constant (this is similar to “local perturbation analysis” [16], in which the equations are analyzed by ignoring the flux law and looking at the evolution of an infinitesimally-small perturbation). This results in the darker blue line in Fig. 5. There we see that the linear feedback model admits only two possibilities: a stable uniform state (when feedback is small relative to the on-rate), and an unstable uniform state which leads to spontaneous polarization (when the feedback is larger). This contradicts our experimental observation of *bistability*.

### 3.4.4 Feedback with saturation

For the uniform steady state to be stable, the attachment rate at constant cytoplasmic concentration has to be smaller than the detachment rate, as shown in the left panel of Fig. 5. At the same time, for bistability, the attachment flux at constant cytoplasmic concentration has to intersect the detachment curve three times (two stable fixed points and one unstable fixed point in between). A simple way to accomplish this is by setting

$$f_A^+(A_1, A_n) = \min\left(A_1 + 2A_n, A^{(\text{Sat})}\right) \rightarrow F_A^+(\hat{A}_1, \hat{A}_n) = \min\left(\hat{A}_1 + 2\hat{A}_n, \hat{A}^{(\text{Sat})}\right). \quad (26)$$

The uniform steady state is stable if  $\hat{A}^{(\text{Sat})} < u = 0.5$ , which provides one constraint on the saturation. The second constraint comes from bistability; the system is only locally bistable at fixed cytoplasmic concentration when  $\hat{A}^{(\text{Sat})}$  is close to the uniform state (if  $\hat{A}^{(\text{Sat})}$  is too small the feed-

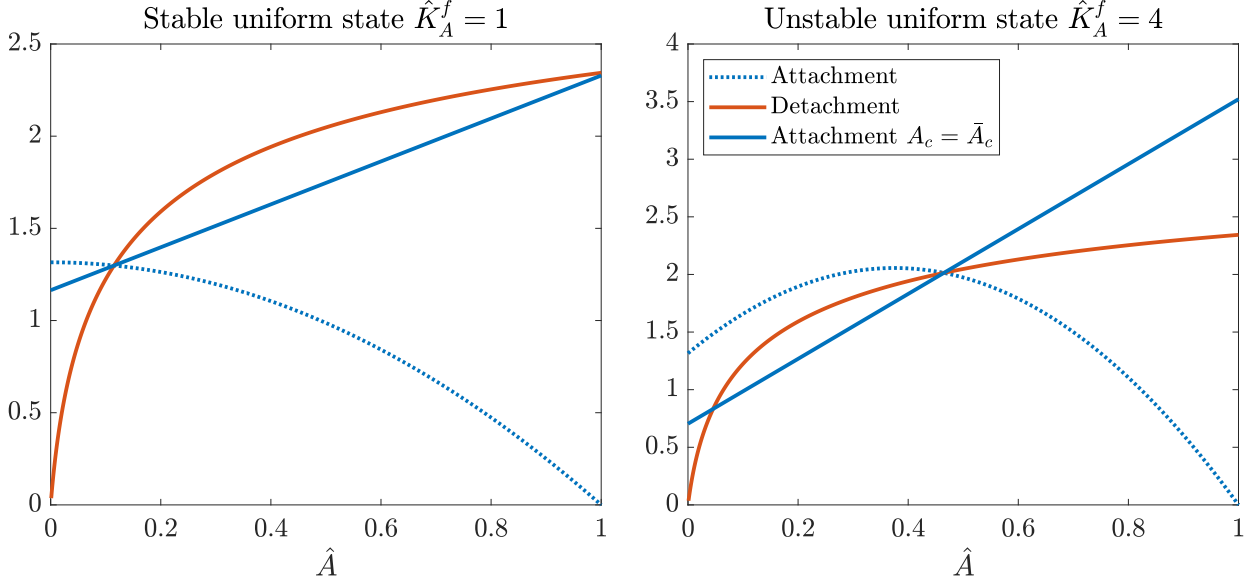


**Figure 5:** Flux plane analysis for *linear feedback* in the stable (left) and unstable (right) case. The stability analysis is determined by how the attachment rate (solid blue line, with constant cytoplasmic concentration) compares to the detachment rate (red) near the steady state.

back becomes essentially constant and cannot generate bistability). Based on these considerations, we set  $\hat{A}^{(\text{Sat})} = 0.35$ .

Once  $\hat{A}^{(\text{Sat})} = 0.35$  is set, there are two unknown parameters, the on rate  $k_A^{\text{on}}$  and the strength of the feedback  $\hat{K}_A^f$ . In Fig. 6, we set these two parameters so that, at the cytoplasmic concentration of the uniform state, the system has a second steady state at roughly 10% of the uniform state. The bistable solution exists for a narrow range of cytoplasmic concentration – when the cytoplasmic concentration is too small or too large, the attachment flux only crosses the detachment flux once, which means that there is no stable state for these cytoplasmic concentrations. Suppose we have the cytoplasmic concentration  $A_c$ , and let  $\hat{A}_1$  and  $\hat{A}_2$  be the two stable states at this concentration. Then in the absence of diffusion, the equation

$$(1-y)\hat{A}_1(\hat{A}_c) + y\hat{A}_2(\hat{A}_c) = 1 - A_c \rightarrow y = \frac{1 - \hat{A}_c - \hat{A}_2}{\hat{A}_1 - \hat{A}_2} \quad (27)$$

defines the fraction of the domain  $y$  that has PAR-3 level  $\hat{A}_2$ .

This completes our parameter selection for the PAR-3 model. The parameters we use going forward are summarized in Table 2.

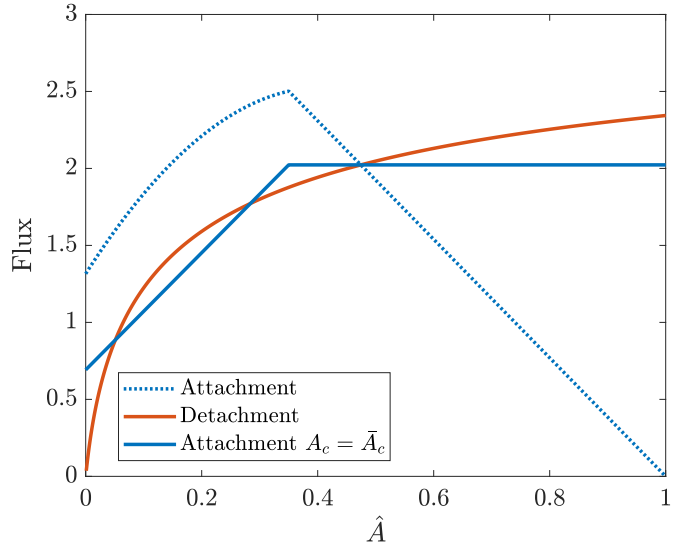


**Figure 6:** Flux plane analysis for capped linear feedback in the bistable case ( $\hat{K}_A^f = 5.5$  and  $k_A^{\text{on}} = 1 \mu\text{m}/\text{s}$ ). The stability analysis is determined by how the attachment rate (solid blue line, with constant cytoplasmic concentration) compares to the detachment rate (red) near the steady state.

Parameter	Description	Value	Units	Ref	Notes
$D_A$	Monomeric PAR-3 diffusivity	0.1	$\mu\text{m}^2/\text{s}$	[21]	
$k_A^{\text{on}}$	Monomeric PAR-3 attachment rate	1	$\mu\text{m}/\text{s}$		Fit for uniform state $\hat{A} = 0.5$
$k_{A,1}^{\text{off}}$	Monomeric PAR-3 detachment rate	3	1/s	[21]	(Fig. 3K)
$\beta$	$k_{A,n}^{\text{off}} = k_{A,1}^{\text{off}} \beta^{n-1}$	0.25		[21]	(Fig. 4E)
$k_A^{\text{dp}}$	PAR-3 depolymerization rate	0.08	1/s	[21]	(Fig. 4E)
$\hat{K}_A^p$	PAR-3 polymerization rate	20			Fit for correct % monomers [21]
$\hat{K}_A^f$	PAR-3 self recruitment rate	5.5			Fit for bistability
$F_A^+$	PAR-3 feedback function	$\min(\hat{A}, 0.35)$		[23]	Stable uniform state
$A^{(\text{Tot})}$	Maximum bound PAR-3 density	–	#/ $\mu\text{m}$		Contained in other unknowns

**Table 2:** Additional parameter values for the PAR-3 model.

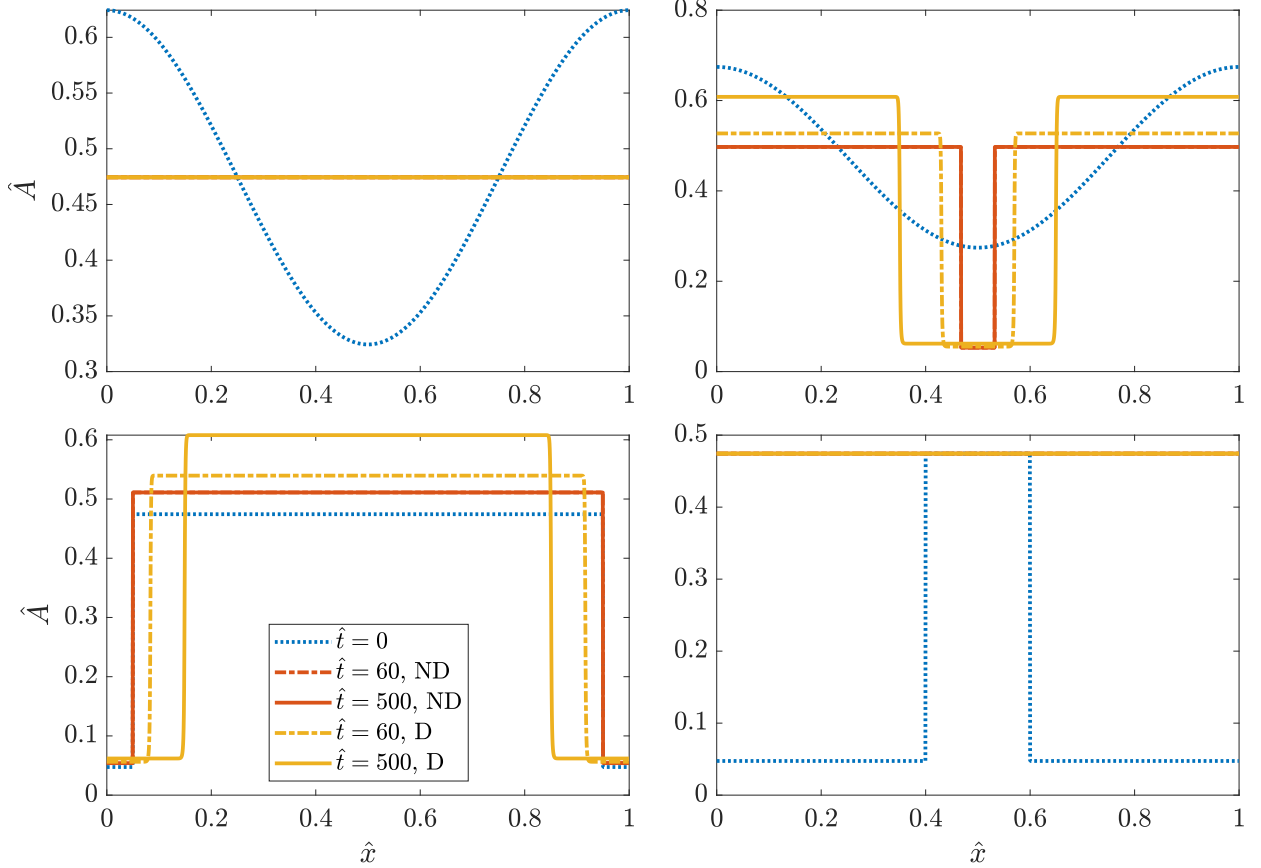


**Figure 7:** Simulating the PAR-3 feedback model with the parameters in Table 2. The initial conditions are shown in dotted blue, and the distribution at  $\hat{t} = 60$  (dashed-dotted lines) and  $\hat{t} = 500$  (solid lines) is shown ( $\hat{t} = 1$  corresponds to 12.5 seconds of real time) both with (yellow) and without (red) diffusion of monomers. In the top row, we make a continuous perturbation from the uniform state, finding that large enough perturbations induce bistability. In the bottom row, we start with a peaked initial profile of large and small size, finding that only larger (than 0.5) initial profiles can lead to bistability.

### 3.5 Simulated steady states with and without diffusion

Let us now look at the dynamics of the model (24) with our constrained parameters. In Figure 7, we run the dynamics forward in time with a variety of initial conditions considering no diffusion and diffusion of monomers. In the top left plot, we see that the uniform steady state is stable, as expected from the stability diagram. But when the perturbation to the uniform state is too large, or when we introduce an asymmetry into the system by depleting PAR-3 in part of the domain, we see bistable dynamics where the small part gravitates to one steady state, while the larger end goes to another. In the bistable region, we observe a posterior concentration which is always roughly 10% of the anterior concentration, as desired (the exact number at steady state is  $0.043/0.51 \approx 9\%$ ). The size of the boundary varies depending on whether we include diffusion or not. When there is no diffusion, the boundary rapidly adjusts (in under 5 minutes) to its stable position, which is dictated only by the initial conditions. When we add diffusion, there is slow relaxation to a unique boundary position which has about 70% enrichment.

In the case when we deplete PAR-3 in part of the domain, the bistable behavior only happens when the initial domain size is sufficiently large. Figure 7 demonstrates this in the bottom row, where we consider initial domains of PAR-3 enrichment of 0.9 (bottom left) and 0.2 (bottom right). We find that when the initial PAR-3 domain of enrichment is larger than 30% of the domain, the system tends to the bistable state, with about 70% of the domain enriched in PAR-3 and 30% at the lower state. When the initial domain of PAR-3 enrichment is too low, however, we find that the flux into the depleted regions is too large, and those regions tend to surpass the smaller bistable steady state and be attracted to the larger uniform one. The higher flux happens because of a larger cytoplasmic concentration (which could result from the initial condition, or from unbinding from the enriched domain if we try to deplete the cytoplasm initially). In any case, the conclusion of Fig. 7 is that there is a uniform steady state, which is the attractor when most of the PAR-3 is initially in the cytoplasm, and a bistable state.

#### 3.5.1 Position of boundary and approach to steady state

Let us now try to understand the position of the boundary. In Fig. 8, we plot the size of the enriched PAR-3 domain over time for various initial boundary positions. We start without diffusion, observing that, for sizes of the enriched PAR-3 domain 0.4 or larger, the cytoplasmic concentration is sufficiently low for a bistable solution to exist (left panel of Fig. 8). When the PAR-3 domain is

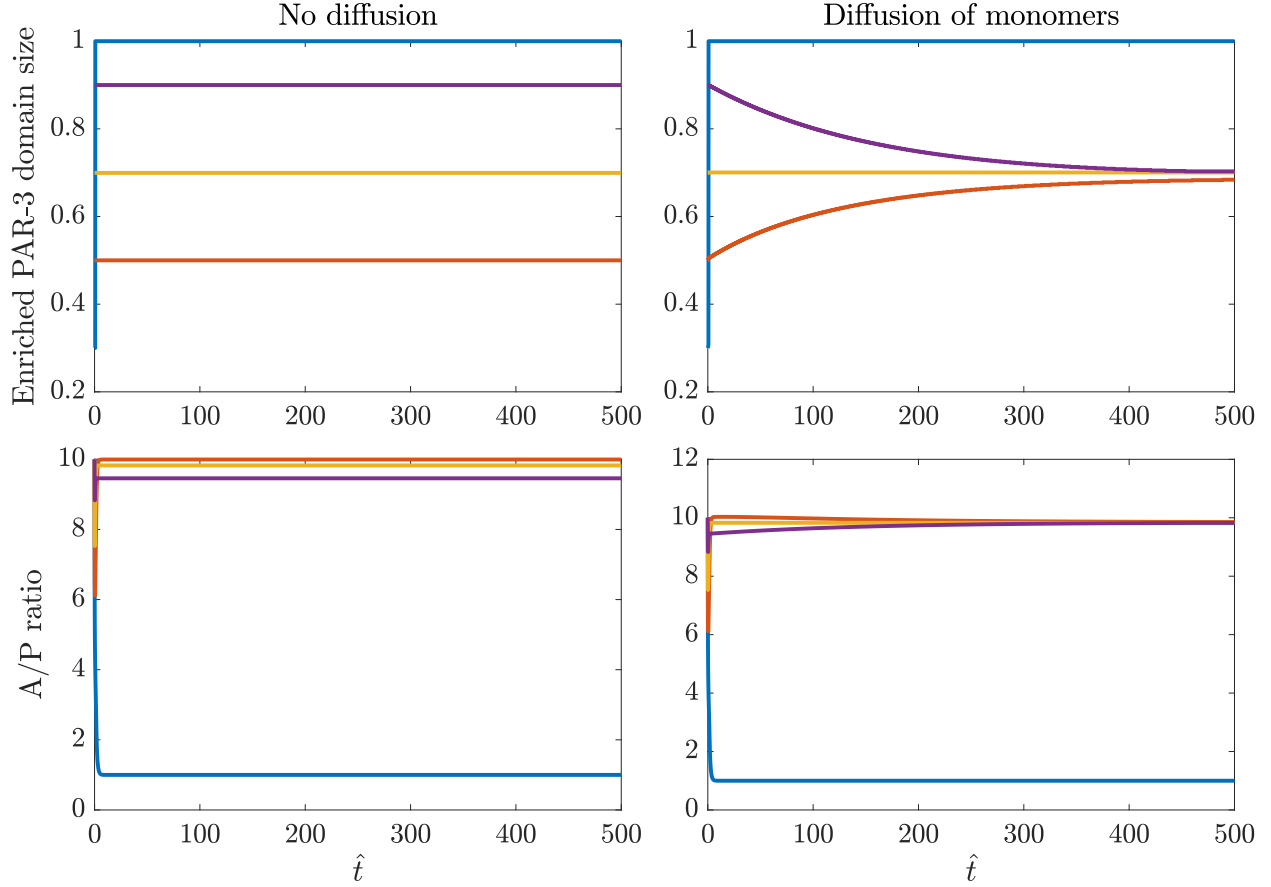
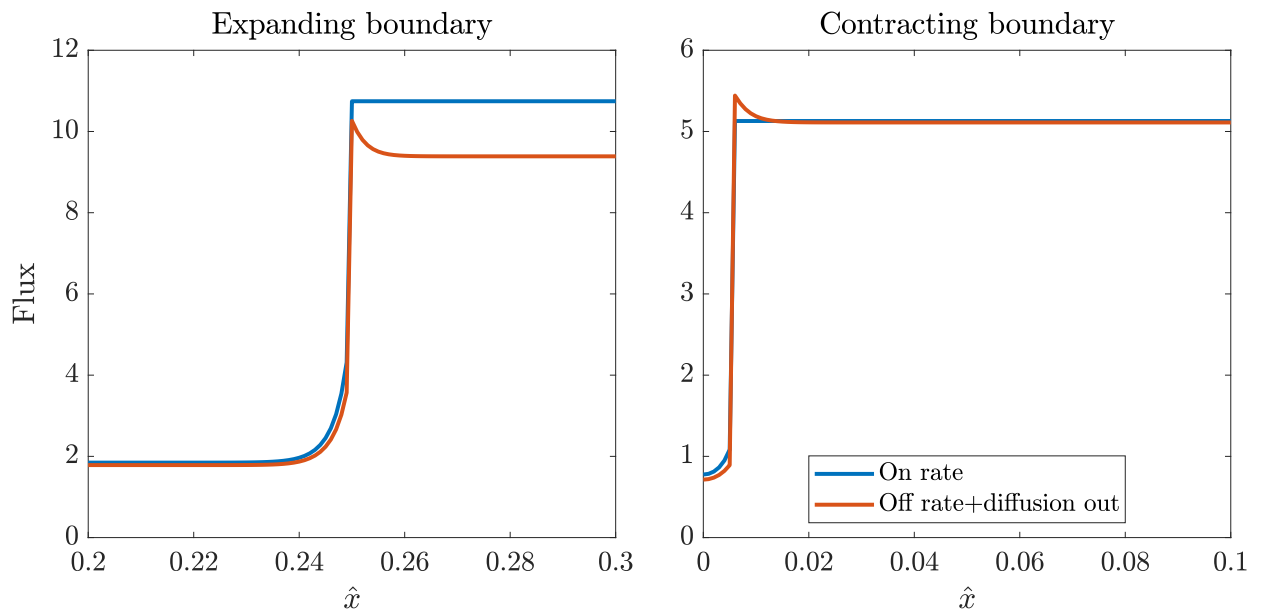


**Figure 8:** Size of PAR-3 domain over time without (left) and with (right) diffusion of monomeric PAR-3. Without diffusion, any boundary position more than 20% enriched PAR-3 is stable, because there exists a solution to (27) where the on rate balances the off rate in both the enriched and depleted regions. When we introduce diffusion, there is an additional constraint in the boundary layer which specifies a unique boundary position.

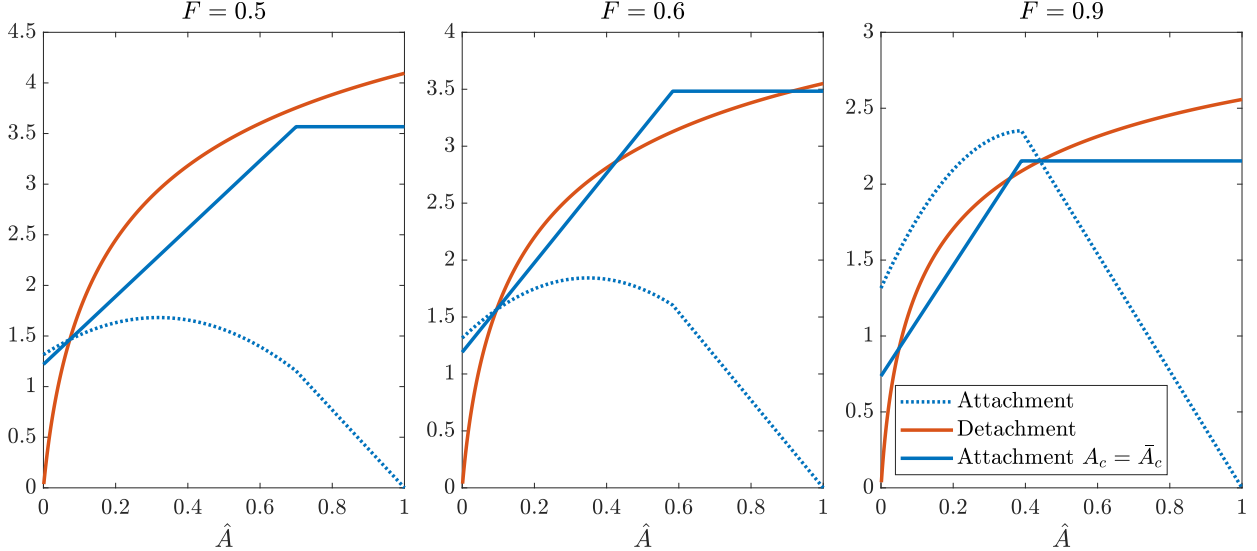
initially too small, the cytoplasmic concentration at steady state would be too high for bistability, and so the uniform state is the only stable one. If the bistable solution exists, then the boundary position does not move in time; any domain size 0.4 or larger appears to be stable. In the absence of diffusion, the A/P ratio is a weak function of the amount of enrichment. Higher domains of enriched PAR-3 give *smaller* A/P ratios, while smaller domains of enrichment give larger ones. This is because the cytoplasmic concentration, which is one part of the slope of the feedback curve, is larger when the enriched domain is smaller.

Figure 8 shows that adding diffusion into the model provides an additional constraint that gives a unique boundary position and A/P ratio. In this case, the right panels of Fig. 8 show that there is a *unique* boundary position and A/P ratio (around 10) that the system tends to, when the diffusive flux in the *boundary layer* balances the net unbinding and binding fluxes. Indeed, when we turn on diffusion, there is diffusion of monomers away from the enrichment zone, and consequently local depletion of monomers at the edge of the enrichment zone (oligomers are not depleted, so the on flux is basically unchanged). There is then an imbalance of flux where the flux from binding is larger than the unbinding flux at the edge of the enrichment zone. If the on-rate dominates diffusion (this is the case when the cytoplasm is enriched), then the boundary will tend to expand. On the other hand, if diffusive fluxes are sufficiently large (cytoplasmic depletion or larger zone of enrichment), then the boundary will contract if diffusive flux outwards overcomes the increased local binding. The unique boundary position is when the diffusive of monomers outward exactly compensates for the slower unbinding rate with diffusion. Figure 9 shows examples of this.

An important observation from Fig. 8 is the *rate* at which the boundary shifts to the steady state. Because the rate of expansion/contraction is controlled by diffusion of monomers, and because the dimensionless diffusivity  $\hat{D}_A \approx 7 \times 10^{-5}$ , the movement of the boundary is quite slow. Indeed, most embryos are in maintenance phase for about 10 minutes, which corresponds to  $\hat{t} = 48$ . During this time, the movement of the boundary is at most 5% of the perimeter, or about 10% of the embryo length. Similar arguments to this were made in [23] to justify the possibility that the uniform steady state is unstable, and that the polarized PAR-3 state (in which PAR-3 is stably enriched on one half of the embryo) [21] might be a transient state that transitions to a large peak if we were to wait long enough. Here we propose that the polarized state of PAR-3 in the absence of PAR-1 is a result of the initial sperm cue, and that, if given long enough, the position of the boundary would relax towards the posterior side.



**Figure 9:** Local depletion by diffusion and consequent expansion/contraction of boundary. These figures show the positive fluxes due to binding (blue) and the negative fluxes due to diffusion and unbinding (red). When the boundary is narrow (left figure), the binding rate is higher due to enriched cytoplasm, and the boundary expands. On the other hand, when the boundary is wider (right figure), the binding rate is locally lower than the off rate + diffusion (note diffusion makes the difference in this case), and the boundary contracts.



**Figure 10:** Examples for when the feedback saturates at  $\hat{A}^{(\text{Sat})} = A_0^{(\text{Sat})}/A^{(\text{Tot})} = 0.35/F$  ( $F$  is the fraction of PAR-3 in the system relative to the default). We show three possible regimes: (left) low uniform steady state with no bistability, (middle) low uniform steady state with bistability, and (right) high uniform steady state with bistability. There is also a fourth regime with an unstable uniform state which is not shown. In the middle regime, the anterior state can become highly enriched at low concentrations, and so the A/P ratio is roughly constant with changing A/P.

### 3.6 Systematic depletion of PAR-3 and how feedback changes

We now systematically tune the oligomerization rate and feedback strength in accordance with a PAR-3 depletion experiment. In light of the scalings in (18c), we consider a fraction of the total PAR-3, denoted by  $F = A^{(\text{Tot})}/A_{\text{WT}}^{(\text{Tot})} < 1$ , then vary the polymerization rate by  $\hat{K}_A^{\text{P}} = 20F$ , and feedback strength via  $\hat{K}_A^{\text{f}} = 5.5F$  (just multiplying the base parameters by the fraction of available PAR-3). The problem here is that we still do not know how to scale the feedback saturation threshold  $\hat{A}^{(\text{Sat})}$  with  $F$ . We consider three hypotheses in this section:

1. The feedback saturates at a fixed *number* of monomers  $A_0^{(\text{Sat})}$ . In this case, the relative saturation point is  $A_0^{(\text{Sat})}/A^{(\text{Tot})}$ , which scales as  $1/F$ . We therefore consider a saturation threshold  $\hat{A}^{(\text{Sat})} = \hat{A}_{\text{WT}}^{(\text{Sat})}/F = 0.35/F$ . Figure 10 shows three examples of this scenario, which correspond to three places on the phase plane. We focus on comparing the middle and right panels. In the middle, we see bistable dynamics, but the increase in the saturation point leads to a *higher* anterior (and posterior) state when  $F = 0.6$  than when  $F = 0.9$ . Thus, this feedback model predicts a constant or increasing A/P ratio as we *decrease* the amount

of PAR-3. This does not match experimental data.

2. The feedback saturates at a fixed *percentage* of monomers  $\hat{A}_0^{(\text{Sat})} = 0.35$ . Examples of this are shown in Fig. 11. Four regimes are shown: (top left) low uniform steady state with no bistability, (top right) low uniform steady state with bistability, (bottom left) unstable uniform state with bistability, (bottom right) high uniform steady state with bistability. This model predicts a decreasing A/P ratio as we decrease the amount of protein ( $F = 0.7$  falls on the boundary of bistability). The main issue with it is that it predicts an unstable uniform state at some intermediate protein amounts (e.g., it predicts spontaneous polarization for  $F = 0.8$ ).
3. The feedback saturates at a fixed percentage (74%, determined from the default parameters) of the uniform state. In this model, we solve for the uniform state  $u$  assuming the feedback is saturated at  $0.74u$ , then substitute to obtain the saturation level in non-uniform states. Examples of this process are shown in Fig. 12. There we see that the uniform state is always stable, and that the A/P asymmetry will increase as  $F$  increases. However, the threshold amount of protein for bistability is quite high. Even with 90% of the protein, we still do not see bistability (middle panel of Fig. 12).
4. We compare these feedback models to a simpler case where we assume a *recruitment asymmetry* is responsible for the A/P ratios. Examples of this are shown in Fig. 13. Our procedure for this is to first fix  $k_A^{\text{on}}$  so that at the default parameter values there is a uniform state with 50% bound protein. We then plot the attachment rate (at constant cytoplasmic concentration) at half the basal on rate, to estimate the “posterior” state. The prediction of this model is that the asymmetry will persist for any arbitrary amount of bound  $\hat{A}$ .

### 3.6.1 Systematic depletion of PAR-3

In Fig. 14, we put our models for feedback together into one summary plot and compare with experimental data. The left plot shows the dependence of the mean oligomer size (at the uniform steady state) on the amount of bound PAR-3; this is a weak function of feedback and primarily a function of polymerization rate. As such, all of our feedback models give results that match the data. The right plot shows the A/P asymmetry as a function of mean oligomer size. It is here that the behavior of our different models diverges strongly. We see that

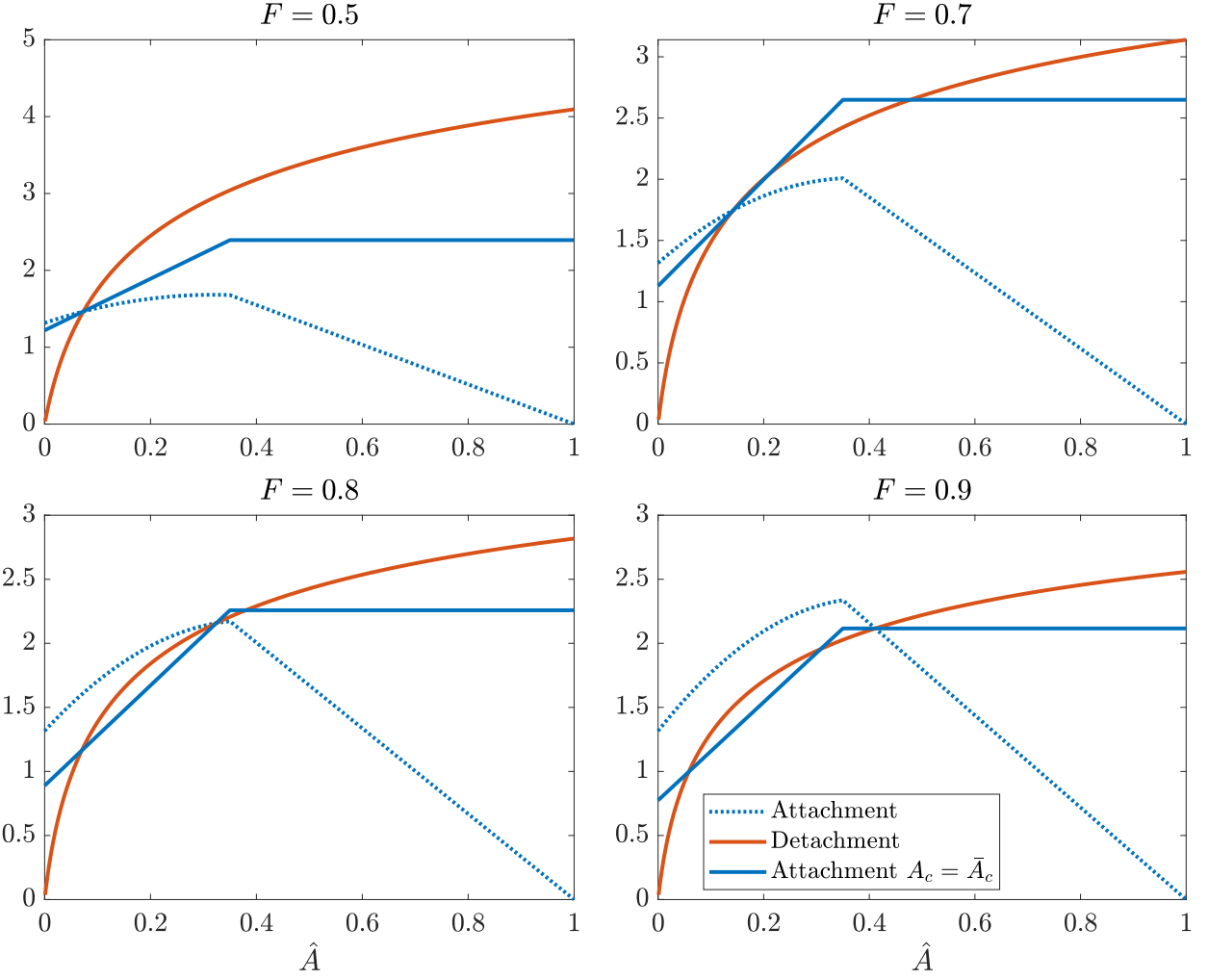


**Figure 11:** Examples for when the feedback saturates at  $\hat{A}^{(\text{Sat})} = \hat{A}_0^{(\text{Sat})} = 0.35$ . We show four possible regimes: (top left) low uniform steady state with no bistability, (top right) low uniform steady state with bistability, (bottom left) unstable uniform state with bistability, (bottom right) high uniform steady state with bistability.  $F$  is the fraction of PAR-3 in the system relative to the default

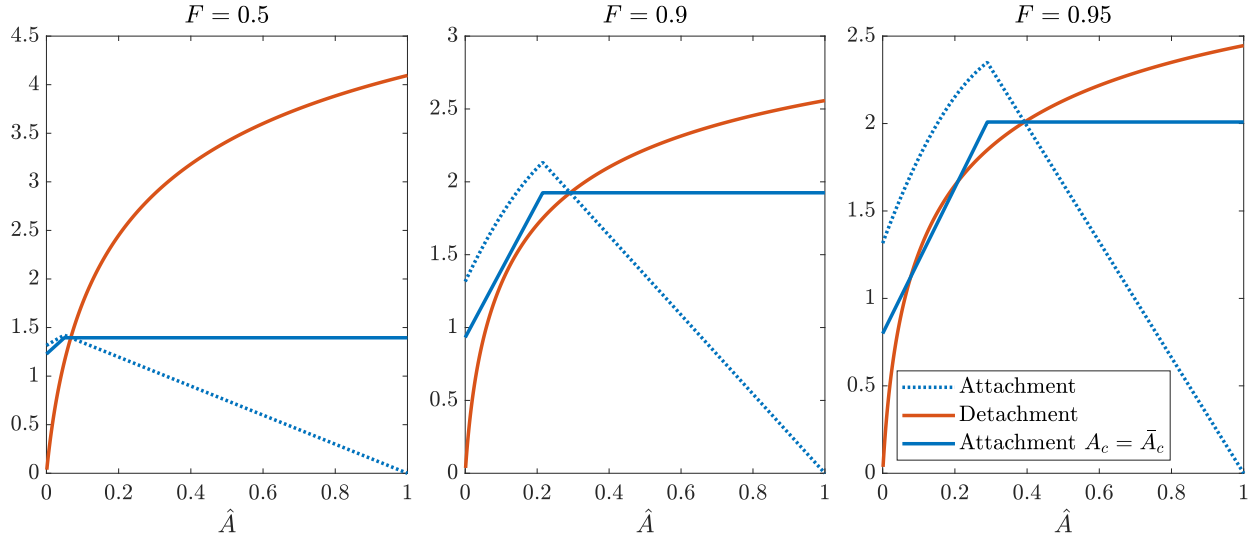


**Figure 12:** Examples for when the feedback saturates at  $\hat{A}^{(\text{Sat})} = 0.74u$  (a fixed percentage of the uniform state). The uniform state is always stable, but there is only a narrow range of protein concentrations that give bistability.

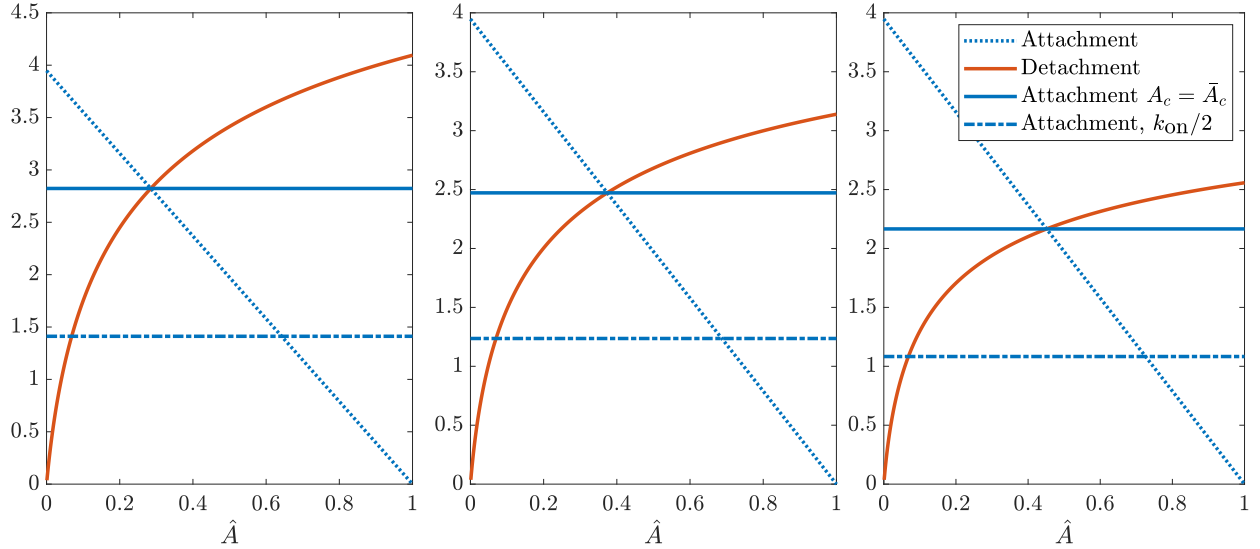


**Figure 13:** Examples for when there is a recruitment asymmetry instead of feedback. We set  $k_A^{\text{on}} = 3 \mu\text{m/s}$  to get 50% bound at the uniform state. This gives the cytoplasmic concentration at uniform steady state, and the solid blue curve is the binding rate at this concentration. We then consider a recruitment asymmetry where the posterior half has  $k_A^{\text{on}} = 1.5 \mu\text{m/s}$ , and draw the binding curve again in dashed-dotted blue. The “posterior state” is the intersection of this curve with the unbinding curve. These plots show  $F = 0.5, 0.7$ , and  $0.9$  from left to right.

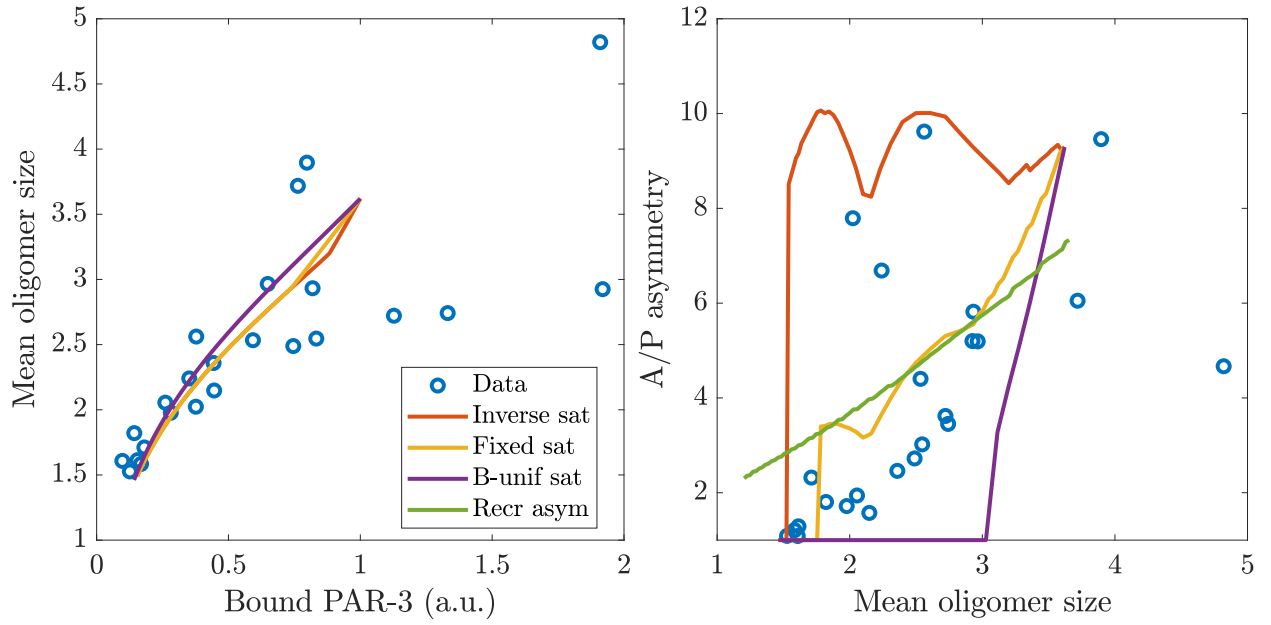


**Figure 14:** PAR-3 depletion experiment. We consider a fraction of the total PAR-3  $x = A^{(\text{Tot})}/A_{\text{WT}}^{(\text{Tot})}$ , then vary the polymerization rate by  $\hat{K}_A^P = 20x$ , and feedback strength according to  $\hat{K}_A^f = 5.5x$  (for  $x = 1$ , these are the base parameters in Table 2). The left plot shows the mean oligomer size (at the uniform state) as a function of the amount of bound PAR-3 at the uniform state. The right plot shows the A/P asymmetry as a function of the mean oligomer size (**in the uniform state, slightly different**). Blue circles are experimental data. The lines show the four models for feedback and asymmetry that we outline in Section 3.6.

1. The feedback model with  $\hat{A}^{(\text{Sat})} = 0.35/F$  (red line) bifurcates from a state with no asymmetry to one where the anterior is 10 times enriched relative to the posterior. The asymmetry is not a strong function of oligomer size (this is expected from Fig. 10).
2. The feedback model with  $\hat{A}^{(\text{Sat})} = 0.35$  (yellow line) has no asymmetry with mean oligomer sizes less than 1.8. Once the mean oligomer size goes above this, there is an asymmetry which generally grows with mean oligomer size (this is also expected from Fig. 11).
3. The feedback model with  $\hat{A}^{(\text{Sat})} = 0.73u$  (fixed fraction of uniform state) has no asymmetry with mean oligomer sizes less than 3. Once the mean oligomer size goes above 3, there is a rapid transition to a large asymmetry (as Fig. 12 showed, this model has only a narrow bistability range).
4. The recruitment asymmetry model has asymmetries which persist even when only monomers are bound to the membrane (mean oligomer size of 1), as expected from Fig. 13.

### 3.6.2 Replicating experimental conditions

Figure 14 looked at PAR-3 depletion around the uniform state using a kind of local perturbation analysis. In this section, we repeat the analysis considering dynamics. Specifically, we first set the fraction  $F$  of total PAR-3, then scale the dimensionless feedback strength and polymerization rate accordingly. We solve for the uniform steady state with these parameters, then initialize a simulation with half the domain at  $\hat{A} = u$  (the “anterior”) and the other half at  $\hat{A} = 0.1u$  (the “posterior”). We then run the dynamics (24) forward in time until we reach  $\hat{t} = 19.2$ , which is 4 minutes of real time, corresponding exactly to the time interval used in experiments. At  $\hat{t} = 19.2$ , we record the mean oligomer size on the anterior and the A/P asymmetry. The results for our different feedback models are shown in Fig. 15

We once again make the following observations:

1. All of the feedback models predict a bifurcation from no asymmetry to a minimal asymmetry. The size of this asymmetry and the point where the bifurcation occurs depend on the model considered.
2. Feedback saturation at a fixed *number* of monomers (red diamonds) predicts a sharp bifurcation from no asymmetry to an asymmetry on the order of 10.

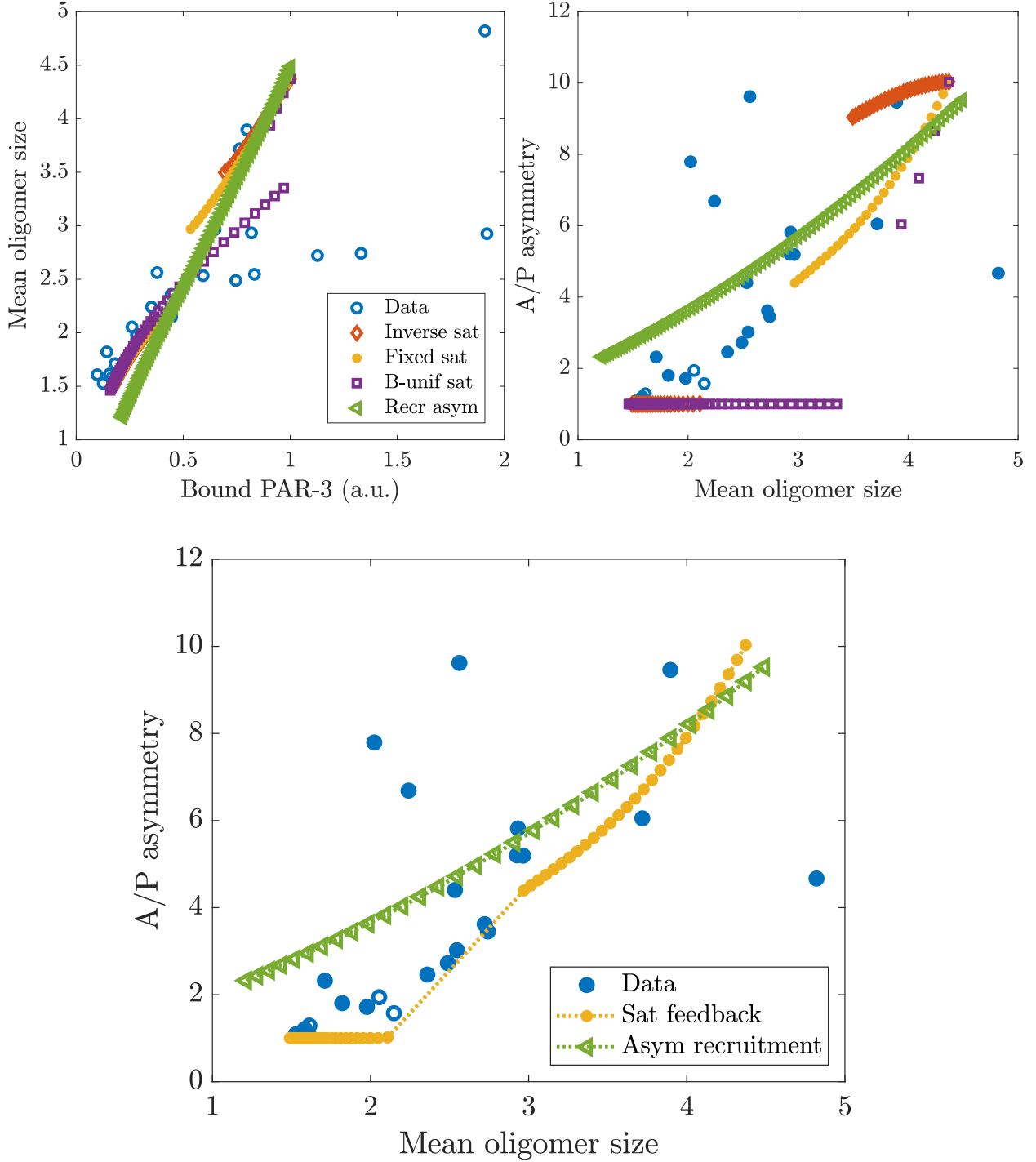


**Figure 15:** Dynamic PAR-3 depletion experiment. We consider a fraction of the total PAR-3  $F$ , then vary the polymerization rate by  $\hat{K}_A^P = 20F$ , and feedback strength according to  $\hat{K}_A^f = 5.5F$  (for  $x = 1$ , these are the base parameters in Table 2). For each set of parameters, we solve for the uniform state  $u$ , then at  $\hat{t} = 0$  set up half the domain at  $\hat{A} = u$  and half the domain at  $\hat{A} = 0.1u$  to mimic the end of “establishment” phase. We then evolve until  $\hat{t} = 19.2$  (4 minutes of real time) and record the A/P asymmetry and mean oligomer size on the anterior. The top plots compare the recruitment models to the data, while the bottom plot is a cleaned-up version for paper main text.

3. Feedback saturation at a fixed *fraction* of monomers (yellow circles) predicts a bifurcation around mean oligomer size of 2.1. The bifurcation is from a small uniform state to an *enriched* anterior state (top right panel in Fig. 11). As such, there is a jump in the mean oligomer size with the bifurcation. The minimum asymmetry is about 4.
4. Feedback saturation just below the uniform state predicts a bifurcation at a mean oligomer size of about 3.5, after which the asymmetry jumps to 6.
5. A model based on recruitment asymmetry (in which case we simply set  $\hat{K}_A^f = 0$ ,  $k_A^{\text{on}} = 3$  on the anterior and  $k_P^{\text{on}} = 1.5$  on the posterior) predicts a persistent asymmetry even as the mean oligomer size drops to 1 (i.e., even without oligomerization). This is not what the experimental data shows.

Thus, while no model for the feedback is perfect, the simplest model (where the feedback saturates at a fixed fraction of PAR-3 bound to the membrane), gives the best match to experimental data, as it reproduces the bifurcation from symmetry to asymmetry, and predicts a minimum asymmetry of about 4. This is the model we use in the main text, and the one we build on going forward.

### 3.6.3 Phase diagram

Ask Charlie and Ed how to do this one.

## 3.7 Including other proteins with mutual inhibition

We now add other proteins to our model of PAR-3, to see if we can reproduce the boundary position in the absence of myosin. We consider the set of proteins shown in Fig. 16. On the anterior side, we have three distinct protein species: PAR-3 (monomers  $A_1$  and oligomers  $A_n$ ), CDC-42 ( $C$ , which is necessary for communication with myosin), and PAR-6/PKC-3 ( $K$ ). While the PAR-6/PKC-3 species may seem redundant, we introduce it to establish a broader gradient of protein that will inhibit the pPARs and ultimately set the lengthscale of protein and myosin gradients. The pPARs (PAR-2, PAR-1, and CHIN-1) can be lumped into one species (denoted by  $P$ ) for this purpose.

The interactions shown in Fig. 16 come from [22, Fig. 2]. Beginning at the top, PAR-3 ( $A$ ) undergoes the oligomerization dynamics that we have already studied in detail. The accumulation of clusters is inhibited by PAR-1 ( $P$ ). We express this by modifying the quasi-steady state

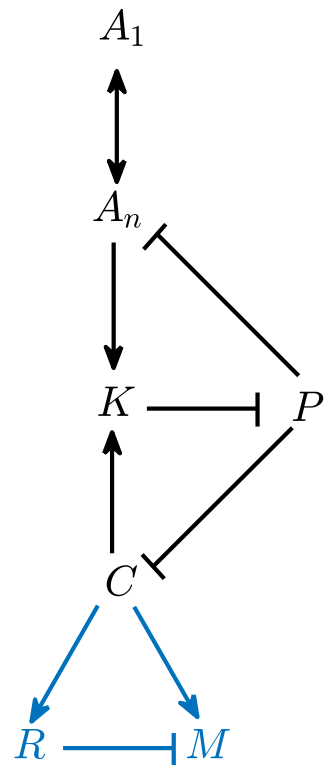


**Figure 16:** Schematic of the biochemistry model. We consider the black parts (biochemistry only) in Section 3.7, and add the blue parts (contractility) in Section 4. On the anterior half,  $A$  represents PAR-3 (in monomer and oligomer form),  $K$  represents the PAR-6/PKC-3 complex, and  $C$  represents CDC-42. The posterior PARs can be represented by a single protein species  $P$ .

approximation (19) to shift the equilibrium amount of oligomers

$$k_A^{\text{dp}} \hat{A}_n + r_{\text{PA}} P \hat{A}_n = k_A^{\text{p}} A_n A_1 \quad (28\text{a})$$

$$\hat{A}_n = \frac{k_A^{\text{p}} A^{(\text{Tot})}}{k_A^{\text{dp}} (1 + \hat{R}_{\text{PA}} \hat{P})} \hat{A}_1 \hat{A}_n = \frac{\hat{K}_A^{\text{p}}}{1 + \hat{R}_{\text{PA}} \hat{P}} := \hat{K}_{AP}^{\text{p}} (\hat{P}) \hat{A}_1 \hat{A}_n, \quad (28\text{b})$$

$$\hat{R}_{\text{PA}} = \frac{r_{\text{PA}} P^{(\text{Tot})}}{k_A^{\text{dp}}}. \quad (28\text{c})$$

Thus, at each point, the fraction of monomers is still a function of the dimensionless polymerization rate, but this rate is a function of the local amount of pPARs on the membrane (the notation  $\hat{K}_{AP}^{\text{p}}$  reflects this). The dimensionless parameter  $\hat{R}_{\text{PA}}$  describes the rate at which pPARs inhibit cluster accumulation relative to the normal rate of depolymerization  $k_A^{\text{dp}}$ .

PAR-3 also gates the association of CDC-42 with PAR-6/PKC-3 ( $K$ ), which is a complex that inhibits all posterior PARs. To model this, we work off the observations in [30], which reveal that PAR-6/PKC-3 are recruited to the membrane by CDC-42, provided that there is a sufficient concentration (roughly 10% of the enriched anterior level) of PAR-3 on the membrane. Absent PAR-3, there is no loading of PAR-6/PKC-3 onto the membrane, so we have no basal rate of loading, and the total loading term is proportional to the CDC-42 concentration times the cytoplasmic concentration of  $K$ , provided  $\hat{A} > \hat{A}_0$ . That is, the on rate for  $\hat{K}$  is equal to  $\hat{C} \delta_{\hat{A} > \hat{A}_0} \hat{K}_{\text{cyto}}$ , where  $\delta_{\hat{A} > \hat{A}_0}(\hat{x})$  is 1 if  $\hat{A}(\hat{x}) > \hat{A}_0(\hat{x})$  and 0 otherwise.

With these preliminaries, we can now formulate the full dimensionless set of equations that describe the interactions in Fig. 16

$$\hat{A}_1 = \frac{1 + 2\hat{A}\hat{K}_{AP}^{\text{p}} - \sqrt{1 + 4\hat{K}_{AP}^{\text{p}}\hat{A}}}{2\hat{A}(\hat{K}_{AP}^{\text{p}})^2} \quad \hat{K}_{AP}^{\text{p}} = \frac{\hat{K}_A^{\text{p}}}{1 + \hat{R}_{\text{PA}} \hat{P}}$$

$$\partial_t \hat{A} = \hat{D}_A \partial_{\hat{x}}^2 \hat{A}_1 + \hat{K}_A^{\text{on}} \left( 1 + \hat{K}_A^{\text{f}} \hat{F}_A^+(\hat{A}) \right) \left( 1 - \int_0^1 \hat{A}(x) dx \right) - \hat{K}_{A,1}^{\text{off}} \frac{\hat{A}_1}{(1 - \beta \hat{K}_{AP}^{\text{p}} \hat{A}_1)^2} \quad (29\text{a})$$

$$\partial_t \hat{C} = \hat{D}_C \partial_{\hat{x}}^2 \hat{C} + \hat{K}_C^{\text{on}} \left( 1 - \int_0^1 \hat{C}(\hat{x}) d\hat{x} \right) - \hat{K}_C^{\text{off}} (1 + \hat{R}_{\text{PC}} \hat{P}) \hat{C} \quad (29\text{b})$$

$$\partial_t \hat{K} = \hat{D}_K \partial_{\hat{x}}^2 \hat{K} + \hat{R}_{\text{ACK}} \hat{C} \delta_{\hat{A} > \hat{A}_0} \left( 1 - \int_0^1 \hat{K}(\hat{x}) d\hat{x} \right) - \hat{K}_K^{\text{off}} \hat{K} \quad (29\text{c})$$

$$\partial_t \hat{P} = \hat{D}_P \partial_{\hat{x}}^2 \hat{P} + \hat{K}_P^{\text{on}} \left( 1 - \int_0^1 \hat{P}(\hat{x}) d\hat{x} \right) - \hat{K}_P^{\text{off}} (1 + \hat{R}_{\text{KP}} \hat{K}) \hat{P} \quad (29\text{d})$$

The first two equations describe the dynamics of PAR-3, and are unchanged from (21) and (24), with the exception that the dimensionless polymerization rate is now a function of  $\hat{A}$  and  $\hat{P}$ . The

Parameter	Description	Value	Units	Ref	Notes
$D_P$	pPAR diffusivity	0.15	$\mu\text{m}^2/\text{s}$	[12]	
$D_K$	PAR-6 diffusivity	0.1	$\mu\text{m}^2/\text{s}$	[28]	
$D_C$	CDC-42 diffusivity	0.1	$\mu\text{m}^2/\text{s}$		Same as PAR-6
$k_P^{\text{off}}$	pPAR detachment rate	$7.3 \times 10^{-3}$	1/s	[12]	
$k_K^{\text{off}}$	PAR-6 detachment rate	0.01	1/s	[28]	
$k_C^{\text{off}}$	CDC-42 detachment rate	0.01	1/s		Same as PAR-6
$k_P^{\text{on}}$	PAR-2 attachment rate	0.13	$\mu\text{m}/\text{s}$	[14]	$P \approx 1$ in enrichment zone
$\hat{R}_{\text{KP}}$	$K$ inhibiting $P$	50			Strong inhibition
$\hat{R}_{\text{PC}}$	$P$ inhibiting $C$	(32)		[30]	CDC/CHIN-1 relationship (Fig. A5)
$k_C^{\text{on}}$	CDC-42 attachment rate	0.1	$\mu\text{m}/\text{s}$		20% bound with inhibition
$\hat{A}_0$	PAR-3 threshold for PAR-6	0.05		[30]	10% anterior level
$\hat{R}_{\text{ACK}}$	$A$ and $C$ creating $K$	0.2			20% bound $K$
$\hat{R}_{\text{PA}}$	$P$ inhibiting $A$	1.5			Fit boundary position

**Table 3:** Additional parameter values for the PAR-3 model when other biochemistry is included.

other three equations describe, respectively, the dynamics of CDC-42 ( $C$ ), PAR-6/PKC-3 ( $K$ ), and all posterior PARs ( $P$ ).

### 3.7.1 Parameters

In (18c), we have already defined the dimensionless parameters that appear in the PAR-3 equations, and their values are assigned in Table 2. The other dimensionless parameters that appear in (29) are

$$\hat{R}_{\text{PA}} = \frac{r_{\text{PA}} P^{(\text{Tot})}}{k_A^{\text{dp}}}, \quad \hat{R}_{\text{PC}} = \frac{r_{\text{PC}} P^{(\text{Tot})}}{k_C^{\text{off}}}, \quad \hat{R}_{\text{ACK}} = \frac{r_{\text{ACK}} C^{(\text{Tot})}}{k_A^{\text{dp}} h}, \quad \hat{R}_{\text{KP}} = \frac{r_{\text{KP}} K^{(\text{Tot})}}{k_P^{\text{off}}} \quad (30\text{a})$$

$$\hat{K}_P^{\text{on}} = \frac{k_P^{\text{on}}}{k_A^{\text{dp}} h}, \quad \hat{K}_C^{\text{on}} = \frac{k_C^{\text{on}}}{k_A^{\text{dp}} h}, \quad \hat{A}_0 = \frac{A_0}{A^{(\text{Tot})}} \quad (30\text{b})$$

$$\hat{D}_P = \frac{D_P}{L^2 k_A^{\text{dp}}}, \quad \hat{D}_C = \frac{D_C}{L^2 k_A^{\text{dp}}}, \quad \hat{D}_K = \frac{D_K}{L^2 k_A^{\text{dp}}}, \quad \hat{K}_P^{\text{off}} = \frac{k_P^{\text{off}}}{k_A^{\text{dp}}}, \quad \hat{K}_K^{\text{off}} = \frac{k_K^{\text{off}}}{k_A^{\text{dp}}}, \quad \hat{K}_C^{\text{off}} = \frac{k_C^{\text{off}}}{k_A^{\text{dp}}} \quad (30\text{c})$$

Among these, the parameters in (30c) are all known from literature, and have been reported in the top half of Table 3. This leaves the seven parameters in (30a) and (30b), which we determine sequentially from the following set of experimental observations:

1. In embryos without myosin flows, roughly 25–30% of the available PAR-2 is bound at steady state [14, Fig. S3]. Because the PAR-2 domain is only 25–30% of the embryo, the concentra-

tion of  $P$  in its enrichment zone must be near 1. We find that  $k_P^{\text{on}} = 0.13 \mu\text{m/s}$ , which is the value obtained from fitting in [14], reproduces this result.

2. In embryos without myosin flows, the level of PAR-2 at the anterior is no more than 5% of the posterior level [14, Fig. 2c]. This sets  $\hat{R}_{\text{KP}} \gg 1$ . We use  $\hat{R}_{\text{KP}} = 50$  for strong inhibition.
3. The parameter  $\hat{R}_{\text{PC}}$  is available from the data in [30]. To obtain it, we solve (29b) at steady state to obtain

$$\hat{C} = \frac{1}{1 + \frac{hk_c^{\text{off}}}{k_C^{\text{on}}} + \frac{\hat{R}_{\text{PC}} k_C^{\text{off}} h}{k_C^{\text{on}}} \hat{P}}. \quad (31)$$

Now according to [30], in a system of units where  $\hat{C} = 1$  when  $\hat{P} = 0$ ,

$$\tilde{C} = \frac{1 + \frac{hk_c^{\text{off}}}{k_C^{\text{on}}}}{1 + \frac{hk_c^{\text{off}}}{k_C^{\text{on}}} + \frac{\hat{R}_{\text{PC}} k_C^{\text{off}} h}{k_C^{\text{on}}} \hat{P}}$$

we have  $\tilde{C} \approx 1/(1 + 13.3\hat{P})$ , which implies that

$$13.3 = \frac{\hat{R}_{\text{PC}} k_C^{\text{off}} h}{k_C^{\text{on}} \left(1 + \frac{hk_c^{\text{off}}}{k_C^{\text{on}}}\right)} = \frac{\hat{R}_{\text{PC}} k_C^{\text{off}} h}{k_C^{\text{on}} + hk_c^{\text{off}}} \rightarrow \hat{R}_{\text{PC}} = 13.3 \left(1 + \frac{k_C^{\text{on}}}{k_C^{\text{off}} h}\right). \quad (32)$$

4. In [14, Fig. S3i], it is reported that roughly 25% of PAR-6 is bound in wild-type embryos. Assuming that CDC-42 has a similar set of properties, we can assume 25% of the protein is bound. Setting  $k_C^{\text{on}} = 0.1 \mu\text{m/s}$  and combining with the inhibition strength (32) gives about 20% bound CDC-42 at steady state.
5. Let's assume  $\hat{C} = 0.25$ ; then we want to set  $\hat{R}_{\text{ACK}}$  to obtain about 25% bound PAR-6 (when there is sufficient PAR-3) as well. Plugging this into the steady state version of (29c), we obtain

$$\hat{R}_{\text{ACK}}(0.25)(0.75) - (0.125)(0.25) = 0 \rightarrow \hat{R}_{\text{ACK}} = 0.17 \approx 0.2.$$

6. In embryos depleted of PAR-1 and CHIN-1, the level of PAR-3 at the anterior is roughly 10% of the posterior, and PAR-6 can load onto the membrane everywhere. We therefore set  $\hat{A}_0 = 0.05$ , as this is 10% of the uniform state.
7. In embryos without myosin flows, the steady state boundary is at 70–75% PAR-3 enrichment [35, Fig. 5B]. This sets  $\hat{R}_{\text{PA}} = 1.5$ .

The way the parameters are set is summarized in Table 3.

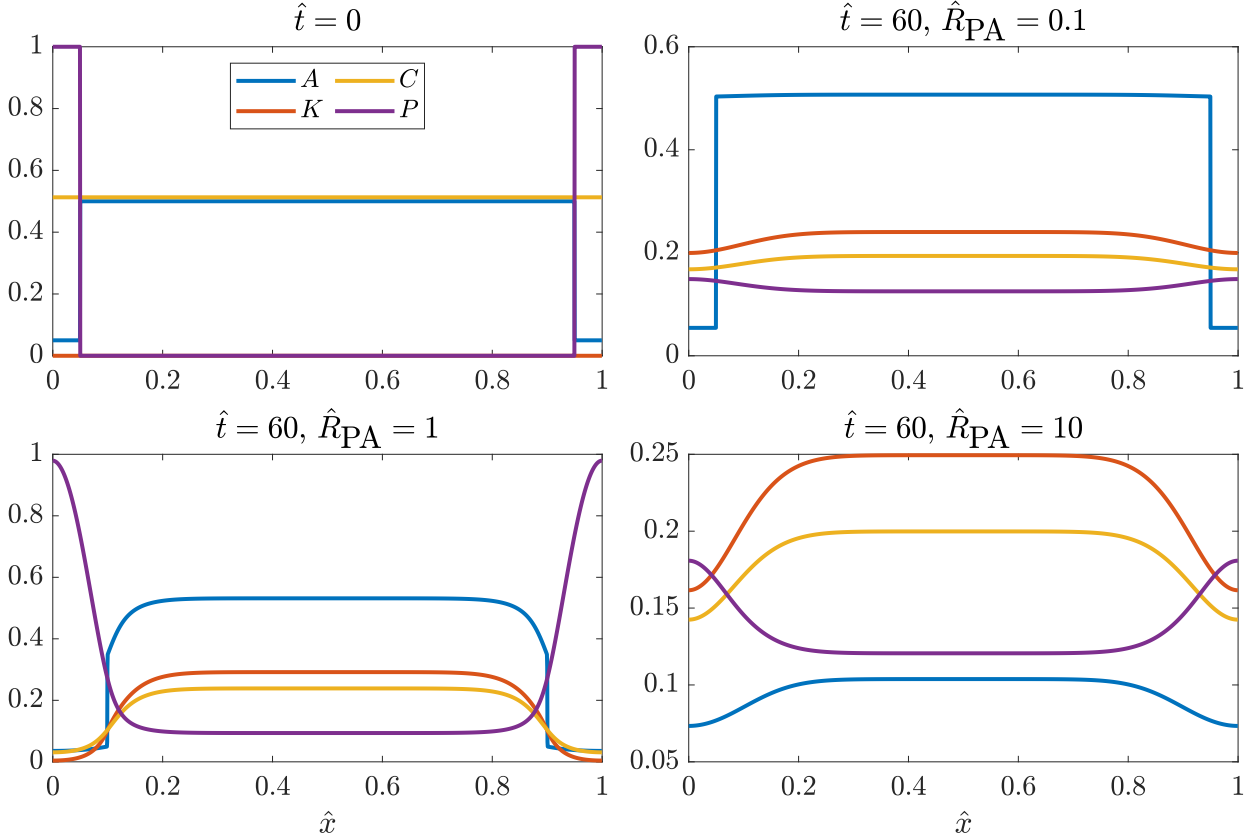


**Figure 17:** Dynamics of biochemistry model (29) with different strengths of PAR-3 cluster inhibition by PAR-1 (parameter  $\hat{R}_{\text{PA}}$ ), all with  $D_A = 0$  (no diffusion of PAR-3). Top right: the initial condition we use for the simulations. PAR-3 ( $A$ ) is enriched in the middle 90% of the embryo, while posterior PARs ( $P$ ) are enriched in the outer 10%. CDC-42 ( $C$ ) is distributed uniformly, and no PAR-6/PKC-3 ( $K$ ) is bound to the membrane. The next three plots show the state at  $\hat{t} = 60$  (about 12.5 minutes of real time) with three different values of  $\hat{R}_{\text{PA}}$ .

### 3.7.2 Regimes of behavior without PAR-3 diffusion

We now try to understand how the biochemistry model (29) can behave for different choices of the PAR-1/PAR-3 inhibition strength  $\hat{R}_{\text{PA}}$ . To accomplish this, we set up an initial condition shown in the top right of Fig. 17, where PAR-3 ( $A$ ) is enriched in the middle 90% of the embryo, while posterior PARs ( $P$ ) are enriched in the outer 10%. CDC-42 ( $C$ ) is distributed uniformly, and no PAR-6/PKC-3 ( $K$ ) is bound to the membrane. We then run the model forward in time until  $\hat{t} = 60$  (12.5 minutes of real time) and look at how the distributions of the proteins evolve.

Based on the results in Fig. 17, we distinguish three different regimes of inhibition:

1. In the regime where  $\hat{R}_{\text{PA}}$  is small (top right), there is not enough inhibition of PAR-3 to

prevent it from accumulating on the posterior at 10% of its anterior level. Because of this, the PAR-6/PKC-3 complex accumulates uniformly on the membrane. Consequently, posterior PARs and CDC-42 all accumulate uniformly.

2. In the regime where  $\hat{R}_{PA}$  is large (bottom right), a small amount of pPARs are sufficient to drive PAR-3 down to its smallest value. Thus, the pPARs outcompete PAR-3, which sets up a state where *all* of the proteins are distributed uniformly.
3. For intermediate values of  $\hat{R}_{PA}$  (bottom left, the exact range is  $0.4 \lesssim \hat{R}_{PA} \lesssim 7$ ), PAR-1 locally drives PAR-3 into its monomer form, which leads to more unbinding. In these regions, the pPARs outcompetes PAR-3 and bind to the membrane. The boundary of the posterior domain expands until it reaches a steady state position (not shown).

### 3.7.3 The boundary position without diffusion of PAR-3

We now try to understand how the boundary position is set in the absence of diffusion. We recall that, for PAR-3 by itself, the boundary position without diffusion is set by the initial condition. But with mutual inhibition, we saw in Fig. 17 that intermediate values of  $\hat{R}_{PA}$  result in shifted boundary positions. Figure 18 shows how this process plays out over times  $\hat{t} = 50$  (10 minutes of real time) to  $\hat{t} = 800$  (over 2.5 hours, which is too long realistically but long enough to establish a steady state). To exaggerate the effect, here we have used the large value of  $\hat{R}_{PA} = 4$ , which at steady state gives  $\alpha = 0.1$  on the posterior (compared to  $\alpha \approx 0.4$  without mutual inhibition) and  $\alpha = 0.74$  on the anterior (compared to  $\alpha \approx 0.75$  without mutual inhibition). We observe contraction of the PAR-3 domain, with a peak that grows over time, and expansion of the PAR-2 domain, with a values for PAR-2 that decrease over time.

The reason the boundary shifts without diffusion of PAR-3 is that PAR-1 shifts the local equilibrium of oligomerization towards the monomer state, driving the depolymerization curve higher and making only one small stable point for the local dynamics. Because of cytoplasmic depletion, the increase in  $A$  and decrease in  $P$  on the anterior domain eventually stops this process, as there is at some point too much  $A$  and not enough  $P$  for  $P$  to win the competition (the decrease in  $P$  comes from both cytoplasmic depletion and cytoplasmic enrichment of CDC-42/PAR-6/PKC-3, which inhibit  $P$ ). To demonstrate that the cytoplasmic dynamics are key to arresting posterior domain expansion, in the right panel of Fig. 18 we simulate with a cytoplasmic pool that is “frozen” at its value at  $\hat{t} = 100$ . The result is an anterior domain which shrinks at a constant rate, until it

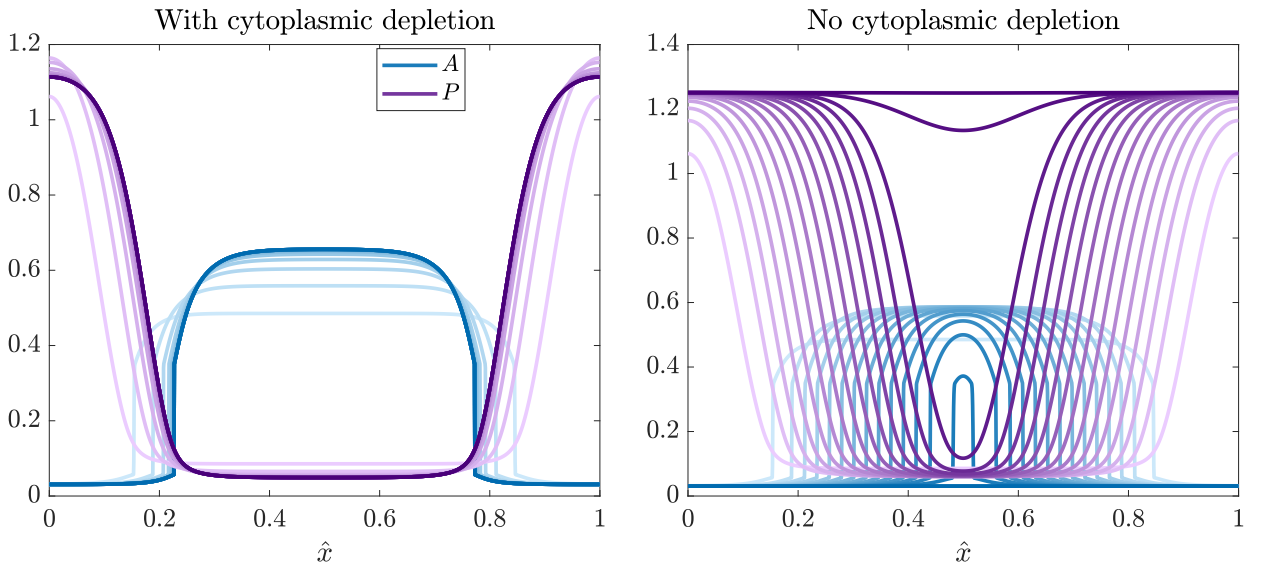


**Figure 18:** Simulating the biochemistry dynamics (29) with (left) and without (right) cytoplasmic depletion. In both cases, we set  $\hat{R}_{\text{PA}} = 4$ , so that we are in the intermediate regime where aPARs and pPARs can coexist on the membrane. We start at the initial condition shown in Fig. 17, then show a sequence of time points from  $\hat{t} = 50$  (the lightest colors) to  $\hat{t} = 800$  (the darkest colors). The left plot shows results with the equations as written, while the right plot removes the cytoplasmic pool updates after  $\hat{t} = 100$ . For clarity of the plot, we show only PAR-3 in blue and pPARs in purple.

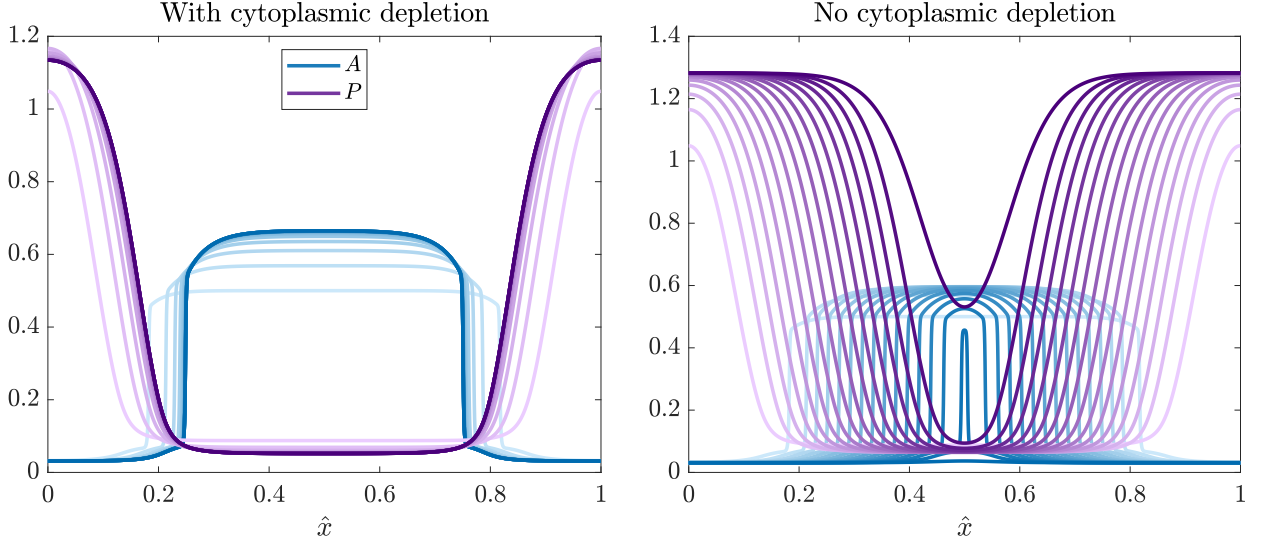


**Figure 19:** Same plot as Fig. 18, but with diffusion of PAR-3 monomers.

is driven to a small state everywhere.

#### 3.7.4 Incorporating diffusion

We now incorporate diffusion of PAR-3 monomers. Naively, we might expect diffusion to prevent the PAR-3 boundary from getting too concentrated, since diffusive flux outward will fight against the tendency of the PAR-3 domain to contract. Figure 19 shows that this is not the case, as the simulations with diffusion are almost identical to those without, in the sense that not accounting for cytoplasmic changes still drives the boundary down to nothing (although at a lower rate than without diffusion). Thus diffusion slows down, but does not stop, the boundary from contracting to zero.

#### 3.7.5 Position of the boundary with correct parameters and diffusion of PAR-3

Show how it evolves from different start positions. We now run the model to steady state and examine the results. We begin with an initial profile where PAR-3 is enriched in a zone, with  $P$  enriched outside of this zone, and the other proteins set uniformly. We find that very small enrichments of PAR-3 (0.1 or less) lead to a state where all proteins are uniform everywhere. A second set of initial sizes (between 0.1 and 0.3) leads to a state where PAR-3 assumes its intrinsic bistable profile, while the other proteins are uniform. If the initial size of the PAR-3 enrichment domain is large enough (40% of the embryo length or larger), we obtain the steady state shown in

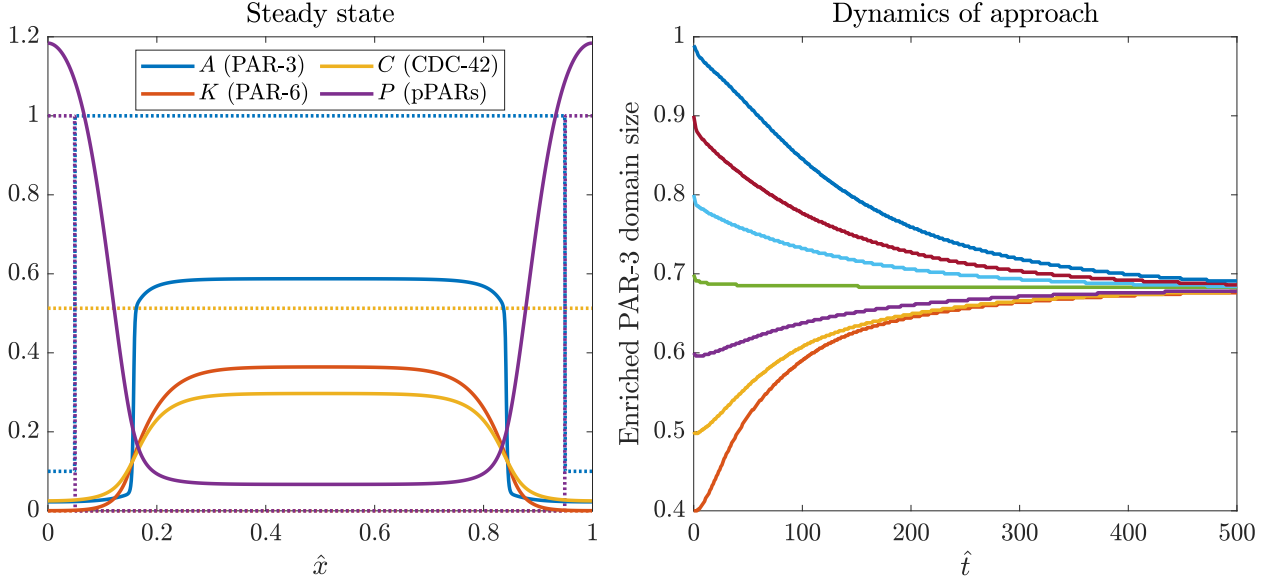


**Figure 20:** Steady state with biochemistry model (29). The left panel shows the steady state we obtain when we start with 40% or more PAR-3 enrichment. We see a domain of PAR-3 taking up about 70% of the embryo, with the other aPARs concentrated in a more narrow zone (the diffusive gradient is larger). The right panel plots the size of the PAR-3 domain as a function of time.

the left panel of Fig. 20. This state has a roughly 70% zone of PAR-3 enrichment, with the other aPARs enriched in a tighter zone inside.

How does the model do in predicting experimental observations we did not fit? The most important one is the posterior/anterior ratio of PAR-3, which at steady state is 4% ( $0.023/0.567$ ). This ratio lines up well with the experimental data in [30, Fig. 4C]. Because of the small ratio, there is no PAR-6 on the posterior pole, as there is not enough PAR-3 to gate the association with CDC-42 and binding to the membrane. The pPAR ratio is about 6% ( $0.068/1.184$ ), which could be compared to experimental data as well.

As in the model with PAR-3 alone, we find that the approach to steady state is quite slow. As shown in the right panel of Fig. 20, an initial zone of 90% PAR-3 enrichment “relaxes” to the steady state on a timescale of roughly  $\hat{t} = 100$ , which is 20 minutes of real time. We need contractility to approach the steady state faster, as we discuss in the next section.

## 4 Coupling contractility to biochemistry

**PAR-3 saturation level has changed slightly.** 4We now present the full model with contractility and all of the biochemistry. The goal of this section is to couple the dynamics of proteins to myosin. We do this through the GTPase CDC-42, which activates myosin and branched actin, as shown in blue in Fig. 16.

## 4.1 Dimensionless equations

To add contractility to the biochemistry system (29), we have to add three things:

1. Introduce myosin and the velocity field that it creates via (9).
2. Incorporate advective terms that ensure that each protein moves with the local cortical velocity [18].
3. Make CDC-42 a promoter of myosin by adding a term of the form  $\hat{R}_{\text{CM}} \hat{C} \hat{M}_{\text{cyto}}$ .

With these steps in mind, we obtain the following dimensionless equations

$$\begin{aligned} \partial_t \hat{A}_1 + \hat{\sigma}_0 \partial_{\hat{x}} (\hat{v} \hat{A}_1) &= \hat{D}_A \partial_{\hat{x}}^2 \hat{A}_1 + \hat{K}_A^{\text{on}} \left( 1 + \hat{K}_A^{\text{f}} F_A^+ (\hat{A}_1, \hat{A}_n) \right) \left( 1 - \int_0^1 \hat{A}(x) d\hat{x} \right) \\ &+ 2\hat{K}_A^{\text{dp}} \left( 1 + \hat{R}_{\text{PA}} \hat{P} \right) \hat{A}_n - 2\hat{K}_A^{\text{p}} \hat{A}_1^2 - \hat{K}_A^{\text{off}} \hat{A}_1 \end{aligned} \quad (33a)$$

$$\partial_t \hat{A}_n + \hat{\sigma}_0 \partial_{\hat{x}} (\hat{v} \hat{A}_n) = \hat{K}_A^{\text{p}} \hat{A}_1^2 - \hat{K}_A^{\text{dp}} \left( 1 + \hat{R}_{\text{PA}} \hat{P} \right) \hat{A}_n \quad (33b)$$

$$\partial_t \hat{C} + \hat{\sigma}_0 \partial_{\hat{x}} (\hat{v} \hat{C}) = \hat{D}_C \partial_{\hat{x}}^2 \hat{C} + \hat{K}_C^{\text{on}} \left( 1 - \int_0^1 \hat{C}(\hat{x}) d\hat{x} \right) - \hat{K}_C^{\text{off}} \left( 1 + \hat{R}_{\text{PC}} \hat{P} \right) \hat{C} \quad (33c)$$

$$\partial_t \hat{K} + \hat{\sigma}_0 \partial_{\hat{x}} (\hat{v} \hat{K}) = \hat{D}_K \partial_{\hat{x}}^2 \hat{K} + \hat{R}_{\text{ACK}} \hat{C} \delta_{\hat{A} > \hat{A}_0} \left( 1 - \int_0^1 \hat{K}(\hat{x}) d\hat{x} \right) - \hat{K}_K^{\text{off}} \hat{K} \quad (33d)$$

$$\partial_t \hat{P} + \hat{\sigma}_0 \partial_{\hat{x}} (\hat{v} \hat{P}) = \hat{D}_P \partial_{\hat{x}}^2 \hat{P} + \hat{K}_P^{\text{on}} \left( 1 - \int_0^1 \hat{P}(\hat{x}) d\hat{x} \right) - \hat{K}_P^{\text{off}} \left( 1 + \hat{R}_{\text{KP}} \hat{K} \right) \hat{P} \quad (33e)$$

$$\partial_t \hat{M} + \hat{\sigma}_0 \partial_{\hat{x}} (\hat{v} \hat{M}) = \hat{D}_M \partial_{\hat{x}}^2 \hat{M} + \hat{K}_M^{\text{on}} \left( 1 + \hat{R}_{\text{CM}} \hat{C} \right) \left( 1 - \int_0^1 \hat{M}(x) dx \right) - \hat{K}_M^{\text{off}} \hat{M} \quad (33f)$$

$$\hat{v} = \hat{\ell}^2 \partial_{\hat{x}}^2 v + \hat{\ell} \partial_{\hat{x}} \hat{\sigma}_a (\hat{M}) \quad (33g)$$

$$R_{\text{CM}} = \frac{r_{\text{CM}} C^{(\text{Tot})}}{k_M^{\text{on}}}, \quad \hat{K}_M^{\text{on}} = \frac{k_M^{\text{on}}}{h k_A^{\text{dp}}}, \quad \hat{K}_M^{\text{off}} = \frac{k_M^{\text{off}}}{h k_A^{\text{dp}}} \quad (33h)$$

These equations do not yet incorporate branched actin.

The last line (33h) defines the key *new* dimensionless parameters relating to myosin. Table 1 gives  $\hat{\sigma}_0$ ,  $\hat{D}_M$ , and  $k_M^{\text{off}}$ , from which we obtain  $\hat{K}_M^{\text{off}}$  (note that we must nondimensionalize time by the same amount in all equations, hence the scaling for  $\hat{K}_M^{\text{off}}$  has changed from (10)). This leaves two parameters which control the myosin profile: the basal rate  $k_M^{\text{on}}$ , and the amount that CDC-42 promotes myosin,  $\hat{R}_{\text{CM}}$ . Our fitting procedure is quite simple:

Parameter	Description	Value	Units	Ref	Notes
$k_M^{\text{on}}$	$M$ attachment rate	0.3	$\mu\text{m}/\text{s}$		20% bound $M$ no CDC
$\hat{R}_{\text{CM}}$	$C$ promoting $M$	1			Correct $M$ profile

**Table 4:** Additional parameters and fitting parameters for coupled model (33).

1. In wild-type and *arx-2* (RNAi) embryos, the minimum amount of bound myosin is 0.2. This sets  $k_M^{\text{on}}$  via  $k_M^{\text{on}}/(k_M^{\text{on}} + k_M^{\text{off}}h) \approx 0.2$ , giving  $k_M^{\text{on}} = 0.3 \mu\text{m}/\text{s}$ .
2. We then fit the parameter  $\hat{R}_{\text{CM}} = 1$  to match the boundary position in *arx-2* (RNAi) embryos, as shown in Fig. 2.

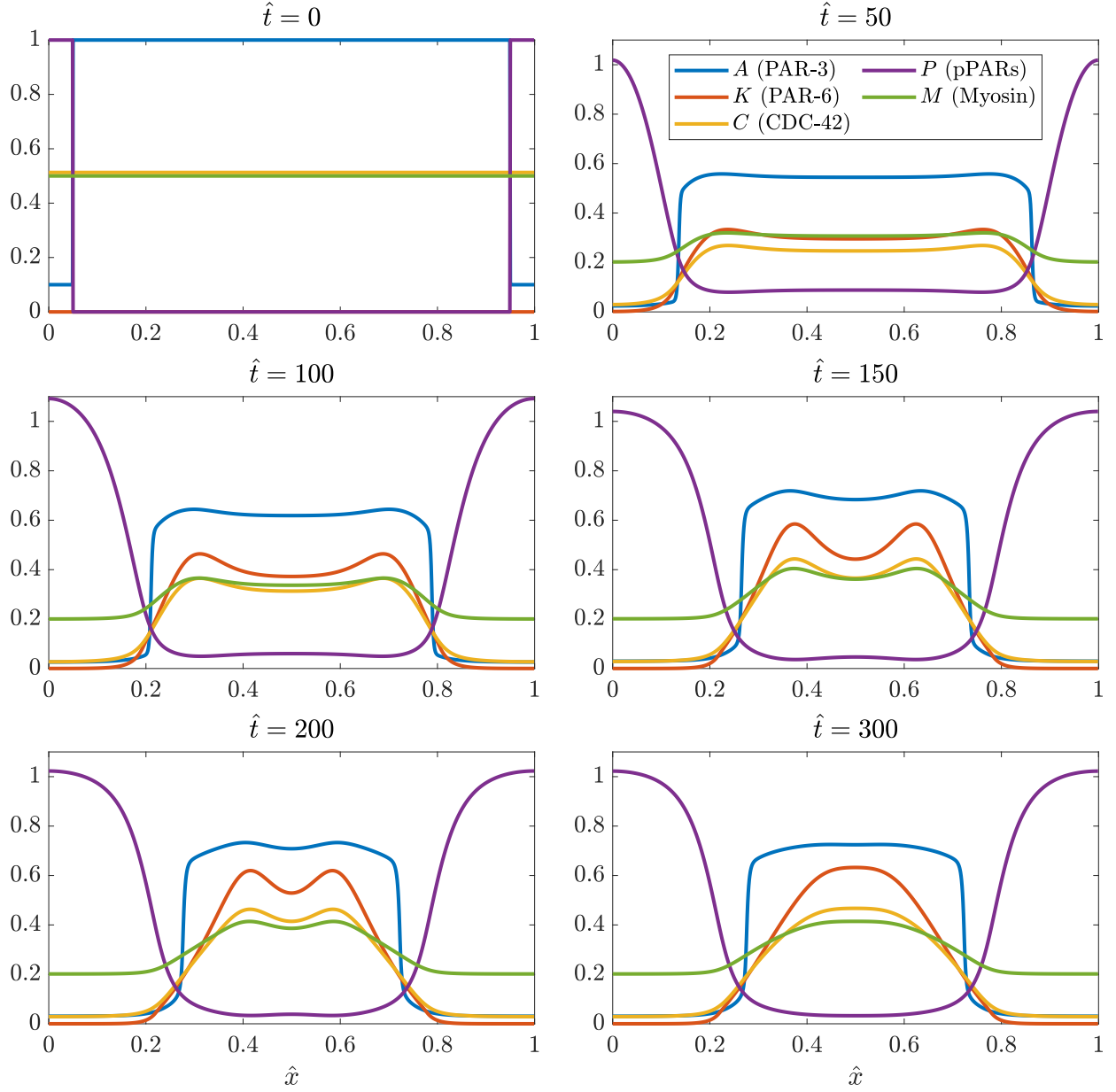
The results are summarized in Table 4.

## 4.2 The steady state compared to experiments

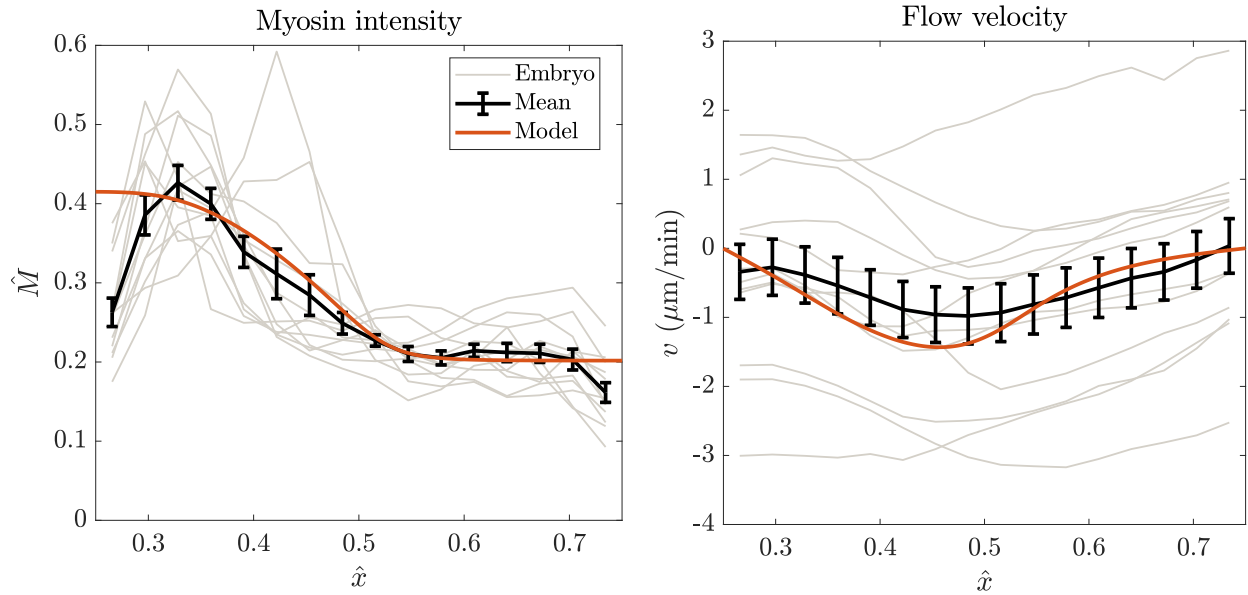
We now look at the performance of this model compared to the experimental data. We simulate the model (33) (with parameters in Tables 1–4) to steady state, and plot the progression in Fig. 21. An initially peaked profile of PAR-2 invades the anterior domain, concentrating anterior PARs in the middle and thereby increasing the concentration of pPARs in the posterior. Once the pPAR boundary advances, the posterior levels start to drop as the cytoplasm gets depleted. This, combined with enrichment of PAR-3 in the interior, leads to a balance where diffusive flux of PAR-3 balances the advective flux that comes in (from a flow which weakens when the pPARs inhibit CDC-42/myosin less). This occurs around  $\hat{t} = 150$  (30 minutes real time). Once the flow comes to a steady state, diffusion takes over, broadening the cap of CDC-42 into a smooth profile.

Figure 22 shows how the myosin intensity and flow profiles compare with the experimental data for hypercontractile *arx-2* embryos. At the correct boundary position, the myosin intensity that we obtain (left panel) matches with the experimental data for *arx-2* (RNAi), but not wild-type embryos, as there is no decrease of myosin near the anterior pole. The flow profile, with a peak negative value at the edge of the anterior domain and a stall point at the anterior cap, reproduces the experimental data in *arx-2* (RNAi) embryos. The incorporation of PAR-6/PKC-3 into the model, which has a diffuse gradient, is what allows us to successfully match the size and spread of the jump in myosin intensities.

How does the approach to steady state compare to previous models? In the left panel of Fig. 23, we show how the model approaches the steady state from an initial zone of PAR-3 enrichment.



**Figure 21:** Time progression of an initially peaked profile of posterior PARs. As shown at  $\hat{t} = 0$  at top left, we begin with 10% depletion of PAR-3, then simulate the model (33) with the parameters in Tables 1–4. The size of the aPAR domain shrinks to a narrow zone (about 40% of the embryo), after which it stops. The stopping point occurs when the diffusion of PAR-3 out of the peak balances the inward flux from flow.



**Figure 22:** Steady state of the model (33), compared to experimental results for *arx-2* (RNAi) embryos. The left panel shows the myosin intensity profile, while the right panel shows the speed of flow. Individual embryos are shown using gray lines, the mean  $\pm$  standard error are shown in black. Results of the model (shifting the anterior pole to  $\hat{x} = 0.25$ ) are overlaid in red.

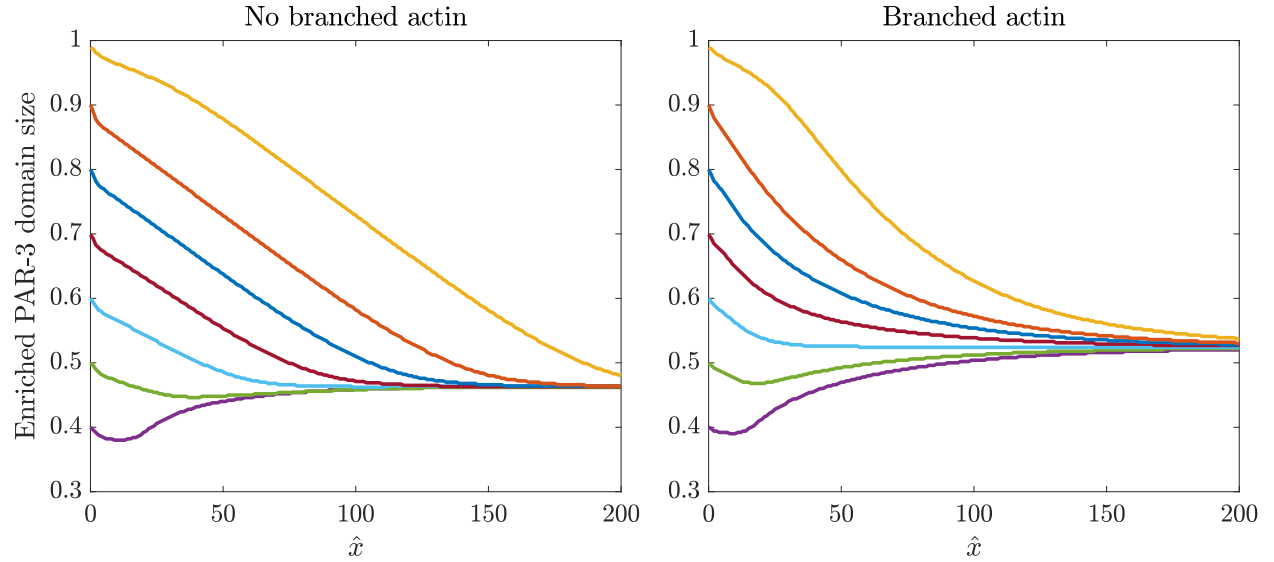


**Figure 23:** Boundary position over time in model (33) without (left panel) and with (right panel, see (34) for adjustments) branched actin. As usual, we start with an initial domain of PAR-3 enrichment, then watch it evolve over time.

As in Fig. 20, where we did not include flows, the initial PAR-3 domain has to be large enough to reach the bistable state. When it is, here we observe approach to the steady state at a roughly linear rate. This means that the approach to steady state is flow, and not diffusion mediated. The approach to steady state occurs over a realistic timescale;  $\hat{t} = 150$  in Fig. 23 corresponds to about 30 minutes of real time.

### 4.3 Incorporating branched actin

Experiments have indicated that wild-type embryos have a way of “halting” the PAR-2 domain growth via branched actin. Our hypothesis is that branched actin is activated above a certain “threshold” of CDC-42, and that branched actin inhibits contractility by inhibiting myosin. We encode these properties in the system of equations by modifying the myosin equation in (33) and adding an additional equation for branched actin, which we represent by  $R$ ,

$$\partial_t \hat{M} + \hat{\sigma}_0 \partial_{\hat{x}} (\hat{v} \hat{M}) = \hat{D}_M \partial_{\hat{x}}^2 \hat{M} + \hat{K}_M^{\text{on}} (1 + \hat{R}_{\text{CM}} \hat{C}) \left( 1 - \int_0^1 \hat{M}(x) dx \right) - \hat{K}_M^{\text{off}} (1 + \hat{R}_{\text{RM}} \hat{R}) \hat{M} \quad (34a)$$

$$\partial_t \hat{R} + \hat{\sigma}_0 \partial_{\hat{x}} (\hat{v} \hat{R}) = \hat{D}_R \partial_{\hat{x}}^2 \hat{R} + \hat{R}_{\text{CR}} (\hat{C} - \hat{C}_R) \delta_{\hat{C} > \hat{C}_R} \left( 1 - \int_0^1 \hat{R}(x) dx \right) - \hat{K}_R^{\text{off}} \hat{R} \quad (34b)$$

Here branched actin is produced above a threshold level  $\hat{C}_R$  of CDC-42, as indicated by the  $\delta$ -function in (34b). Once produced, branched actin inhibits myosin as in (34a). We assume for the moment that branched actin has the same diffusivity ( $0.05 \mu\text{m}^2/\text{s}$ ) and unbinding rate ( $0.12/\text{s}$ ) as myosin.

#### 4.3.1 Additional parameters

There are four new parameters in this model that are unknown:

- $\hat{R}_{\text{CM}}$ , which is the rate at which CDC-42 produces myosin. Because the myosin intensities in wild-type and *arx-2* embryos have roughly the same mean, if branched actin inhibits myosin in these embryos, the rate at which CDC-42 produces myosin must be higher. We therefore set  $\hat{R}_{\text{CM}} = 3$ , which is three times the value we used in the previous section.
- The threshold  $C_R$  is set by examining the steady state in Fig. 21 without branched actin. There we see that, at late times, CDC-42 goes from about 0.05 in the posterior to 0.45 in the anterior. To block contractility, we set  $C_R = 0.2$ .

- The rate at which CDC-42 produces branched actin sets the amount of bound branched actin. This amount is arbitrary, since what matters is not the amount of branched actin but the total amount of myosin inhibition. We set  $\hat{R}_{\text{CR}} = 10$  to get a profile on the same scale as the other aPARs (to make our plots look nice).
- We set the rate at which branched actin blocks myosin  $\hat{R}_{\text{RM}} = 1.5$ , which is the parameter we use to control the dynamics, to reproduce the boundary position in wild type embryos.

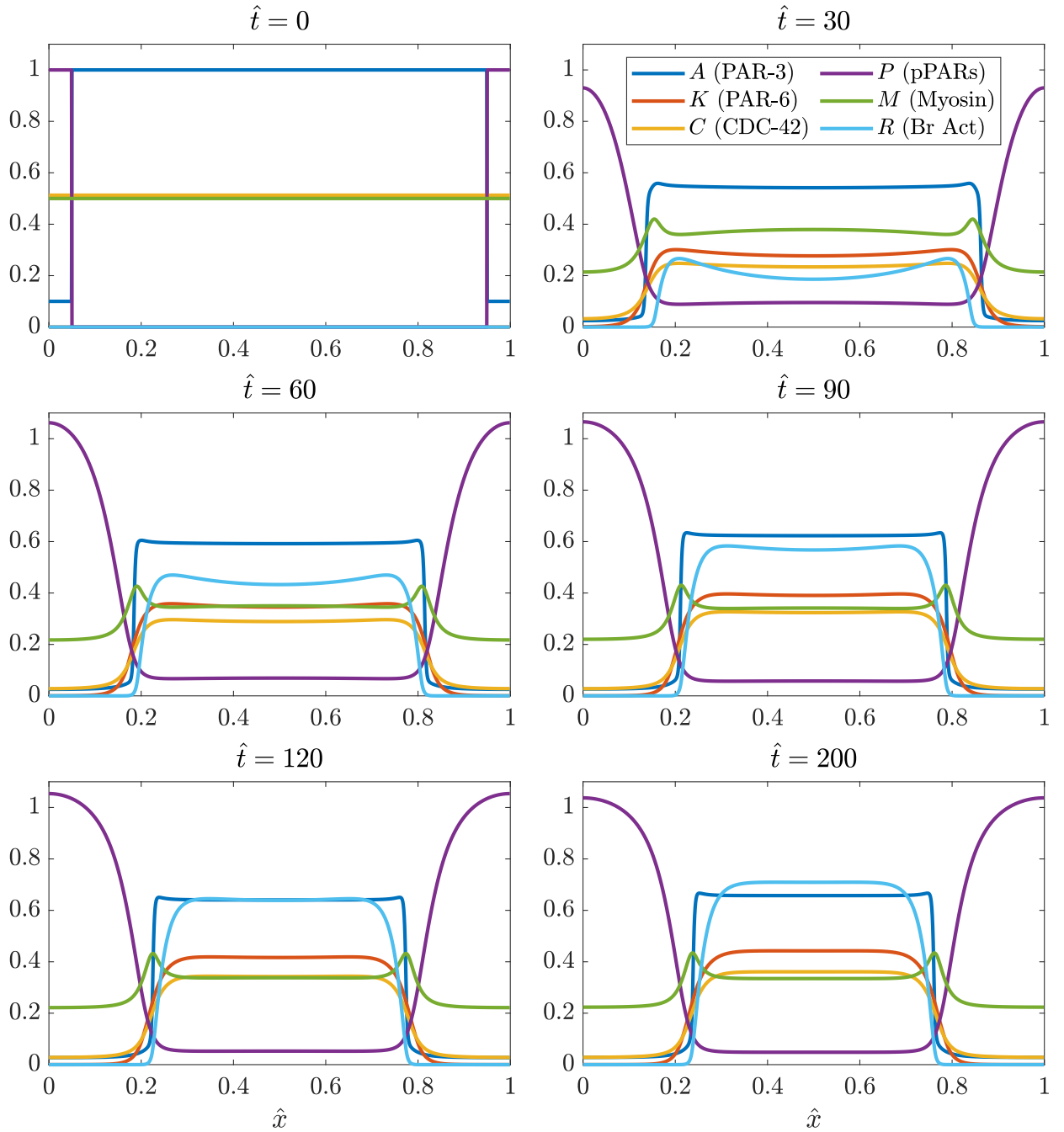
### 4.3.2 Dynamics

Figure 24 shows the dynamics of the approach to steady state for (33) augmented with the branched actin model (34). We see initially the same dynamics as in Fig. 21, with pPARs inhibiting CDC-42 and myosin, which produces an inward flow. However, once the CDC-42 concentration (yellow) gets high enough, branched actin (cyan) starts to be produced and inhibit contractility. This makes the myosin profile decrease, and stalls flow and movement of the boundary. The right panel of Fig. 23 shows that the overall timescale of contraction is about 10–20 minutes ( $\hat{t} = 100$  is 20 minutes of real time).

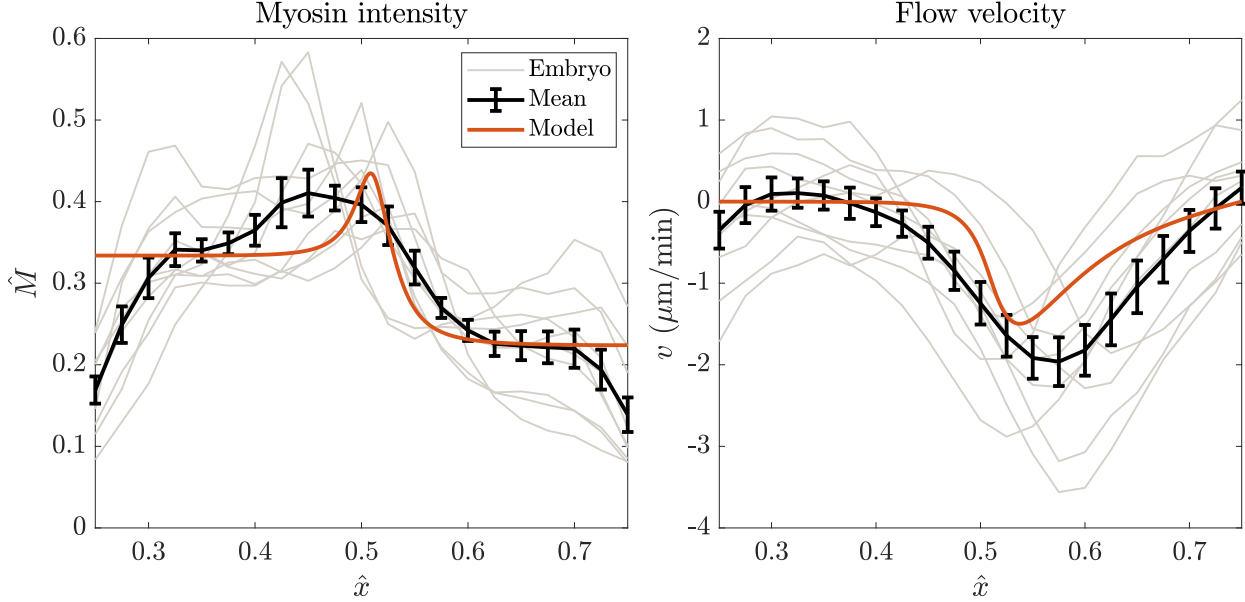
### 4.3.3 Steady state vs. experiments

Figure 25 shows how our modeled steady state compares to wild-type embryos. Qualitatively, the results match: the myosin intensity displays a peak at the anterior cap, then drops off to a level midway between the peak anterior and posterior levels at the anterior pole. The flow also exhibits a maximum off of the anterior cap, then rapidly transitions to a stall point at the edge of the anterior domain.

Quantitatively, our results almost match up with the experiments, but leave a little to be desired. The issue is the lengthscale on which the drop in myosin occurs. Because branched actin is only active on the anterior cap, the lengthscale on which it goes from zero to its peak value is quite small (controlled by the diffusivity, which here is set equal to the diffusivity of myosin; see the last panel of Fig. 25). As such, the myosin is inhibited quickly in the model, and the profile rapidly drops to a flat level in the anterior. This is *not* what is observed in experiments, where we see a more gradual decrease (although the individual embryos do show rapid decreases). The result of this in the flow field is a slightly smaller absolute velocity and a smaller lengthscale once again (relative to the experimental data).



**Figure 24:** Time progression of an initially peaked profile of posterior PARs. As shown at  $\hat{t} = 0$  at the top left, we begin with 10% depletion of PAR-3, then simulate the model (33) *with branched actin* as in (34). The size of the aPAR domain initially shrinks rapidly, and then stalls as branched actin (cyan) starts to inhibit contractility.



**Figure 25:** Steady state of the model (33) with branched actin model (34), compared to experimental results for wild-type embryos. The left panel shows the myosin intensity profile, while the right panel shows the speed of flow. Individual embryos are shown using gray lines, the mean  $\pm$  standard error are shown in black. Results of the model (shifting the anterior pole to  $\hat{x} = 0.25$ ) are overlaid in red.

## References

- [1] Alexander Beatty, Diane G Morton, and Kenneth Kemphues. Par-2, lgl-1 and the cdc-42 gap chin-1 act in distinct pathways to maintain polarity in the *C. elegans* embryo. *Development*, 140(9):2005–2014, 2013.
- [2] Justin S Bois, Frank Jülicher, and Stephan W Grill. Pattern formation in active fluids. *Bio-physical Journal*, 100(3):445a, 2011.
- [3] Adrian A Cuenca, Aaron Schetter, Donato Aceto, Kenneth Kemphues, and Geraldine Seydoux. Polarization of the *C. elegans* zygote proceeds via distinct establishment and maintenance phases. 2003.
- [4] Adriana T Dawes and David Iron. Cortical geometry may influence placement of interface between par protein domains in early *Caenorhabditis elegans* embryos. *Journal of theoretical biology*, 333:27–37, 2013.

- [5] Adriana T Dawes and Edwin M Munro. Par-3 oligomerization may provide an actin-independent mechanism to maintain distinct par protein domains in the early *caenorhabditis elegans* embryo. *Biophysical journal*, 101(6):1412–1422, 2011.
- [6] Evan B Dewey, Danielle T Taylor, and Christopher A Johnston. Cell fate decision making through oriented cell division. *Journal of developmental biology*, 3(4):129–157, 2015.
- [7] Daniel J Dickinson, Francoise Schwager, Lionel Pintard, Monica Gotta, and Bob Goldstein. A single-cell biochemistry approach reveals par complex dynamics during cell polarization. *Developmental cell*, 42(4):416–434, 2017.
- [8] Leah Edelstein-Keshet and G Bard Ermentrout. Models for the length distributions of actin filaments: I. simple polymerization and fragmentation. *Bulletin of mathematical biology*, 60(3):449–475, 1998.
- [9] Bijan Etemad-Moghadam, Su Guo, and Kenneth J Kemphues. Asymmetrically distributed par-3 protein contributes to cell polarity and spindle alignment in early *c. elegans* embryos. *Cell*, 83(5):743–752, 1995.
- [10] Wan Jun Gan and Fumio Motegi. Mechanochemical control of symmetry breaking in the *caenorhabditis elegans* zygote. *Frontiers in Cell and Developmental Biology*, 8:619869, 2021.
- [11] Raphaela Geßele, Jacob Halatek, Laeschkir Würthner, and Erwin Frey. Geometric cues stabilise long-axis polarisation of par protein patterns in *c. elegans*. *Nature communications*, 11(1):539, 2020.
- [12] Nathan W Goehring, Philipp Khuc Trong, Justin S Bois, Debanjan Chowdhury, Ernesto M Nicola, Anthony A Hyman, and Stephan W Grill. Polarization of par proteins by advective triggering of a pattern-forming system. *Science*, 334(6059):1137–1141, 2011.
- [13] Bob Goldstein and Ian G Macara. The par proteins: fundamental players in animal cell polarization. *Developmental cell*, 13(5):609–622, 2007.
- [14] Peter Gross, K Vijay Kumar, Nathan W Goehring, Justin S Bois, Carsten Hoege, Frank Jülicher, and Stephan W Grill. Guiding self-organized pattern formation in cell polarity establishment. *Nature physics*, 15(3):293–300, 2019.

- [15] Jacob Halatek, Fridtjof Brauns, and Erwin Frey. Self-organization principles of intracellular pattern formation. *Philosophical Transactions of the Royal Society B: Biological Sciences*, 373(1747):20170107, 2018.
- [16] William R Holmes, May Anne Mata, and Leah Edelstein-Keshet. Local perturbation analysis: a computational tool for biophysical reaction-diffusion models. *Biophysical journal*, 108(2):230–236, 2015.
- [17] Niv Ierushalmi and Kinneret Keren. Cytoskeletal symmetry breaking in animal cells. *Current Opinion in Cell Biology*, 72:91–99, 2021.
- [18] Rukshala Illukkumbura, Nisha Hirani, Joana Borrego-Pinto, Tom Bland, KangBo Ng, Lars Hubatsch, Jessica McQuade, Robert G Endres, and Nathan W Goehring. Design principles for selective polarization of par proteins by cortical flows. *Journal of Cell Biology*, 222(8), 2023.
- [19] Kenneth J Kemphues, James R Priess, Diane G Morton, and Niansheng Cheng. Identification of genes required for cytoplasmic localization in early *c. elegans* embryos. *Cell*, 52(3):311–320, 1988.
- [20] Natalia Kravtsova and Adriana T Dawes. Actomyosin regulation and symmetry breaking in a model of polarization in the early *caenorhabditis elegans* embryo: symmetry breaking in cell polarization. *Bulletin of mathematical biology*, 76:2426–2448, 2014.
- [21] Charles F Lang, Alexander Anneken, and Edwin Munro. Oligomerization and feedback on membrane recruitment stabilize par-3 asymmetries in *c. elegans* zygotes. *bioRxiv*, pages 2023–08, 2023.
- [22] Charles F Lang and Edwin Munro. The par proteins: from molecular circuits to dynamic self-stabilizing cell polarity. *Development*, 144(19):3405–3416, 2017.
- [23] Charles F Lang and Edwin M Munro. Oligomerization of peripheral membrane proteins provides tunable control of cell surface polarity. *Biophysical Journal*, 121(23):4543–4559, 2022.
- [24] Jean-Léon Maître, Hervé Turlier, Rukshala Illukkumbura, Björn Eismann, Ritsuya Niwayama, François Nédélec, and Takashi Hiiragi. Asymmetric division of contractile domains couples cell positioning and fate specification. *Nature*, 536(7616):344–348, 2016.

- [25] Alex Mogilner, Jun Allard, and Roy Wollman. Cell polarity: quantitative modeling as a tool in cell biology. *Science*, 336(6078):175–179, 2012.
- [26] Yoichiro Mori, Alexandra Jilkine, and Leah Edelstein-Keshet. Wave-pinning and cell polarity from a bistable reaction-diffusion system. *Biophysical journal*, 94(9):3684–3697, 2008.
- [27] Edwin Munro, Jeremy Nance, and James R Priess. Cortical flows powered by asymmetrical contraction transport par proteins to establish and maintain anterior-posterior polarity in the early *c. elegans* embryo. *Developmental cell*, 7(3):413–424, 2004.
- [28] François B Robin, William M McFadden, Baixue Yao, and Edwin M Munro. Single-molecule analysis of cell surface dynamics in *caenorhabditis elegans* embryos. *Nature methods*, 11(6):677–682, 2014.
- [29] Arnab Saha, Masatoshi Nishikawa, Martin Behrndt, Carl-Philipp Heisenberg, Frank Jülicher, and Stephan W Grill. Determining physical properties of the cell cortex. *Biophysical journal*, 110(6):1421–1429, 2016.
- [30] Anne Sailer, Alexander Anneken, Younan Li, Sam Lee, and Edwin Munro. Dynamic opposition of clustered proteins stabilizes cortical polarity in the *c. elegans* zygote. *Developmental cell*, 35(1):131–142, 2015.
- [31] Stephanie Schonegg and Anthony A Hyman. Cdc-42 and rho-1 coordinate acto-myosin contractility and par protein localization during polarity establishment in *c. elegans* embryos. 2006.
- [32] Filipe Tostevin and Martin Howard. Modeling the establishment of par protein polarity in the one-cell *c. elegans* embryo. *Biophysical journal*, 95(10):4512–4522, 2008.
- [33] Philipp Khuc Trong, Ernesto M Nicola, Nathan W Goehring, K Vijay Kumar, and Stephan W Grill. Parameter-space topology of models for cell polarity. *New Journal of Physics*, 16(6):065009, 2014.
- [34] Yu Chung Tse, Michael Werner, Katrina M Longhini, Jean-Claude Labbe, Bob Goldstein, and Michael Glotzer. Rhoa activation during polarization and cytokinesis of the early *caenorhabditis elegans* embryo is differentially dependent on *nop-1* and *cyk-4*. *Molecular biology of the cell*, 23(20):4020–4031, 2012.

- [35] Seth Zonies, Fumio Motegi, Yingsong Hao, and Geraldine Seydoux. Symmetry breaking and polarization of the *c. elegans* zygote by the polarity protein par-2. *Development*, 137(10):1669–1677, 2010.